

<sup>1</sup>  
<sup>2</sup> Susceptible host dynamics explain pathogen resilience to  
<sup>3</sup> perturbations

<sup>4</sup>

<sup>5</sup> Sang Woo Park, . . . , Bryan T. Grenfell, Sarah Cobey

## <sup>6</sup> Abstract

<sup>7</sup> Major priority for epidemiological research in the time of anthropogenic change is  
<sup>8</sup> understanding how infectious disease dynamics respond to perturbations. Interven-  
<sup>9</sup> tions to slow the spread of SARS-CoV-2 significantly disrupted the transmission  
<sup>10</sup> of other human pathogens. As interventions lifted, whether and when respiratory  
<sup>11</sup> pathogens would eventually return to their pre-pandemic dynamics remains to be  
<sup>12</sup> answered. Here, we present a framework for estimating pathogen resilience based on  
<sup>13</sup> how fast epidemic patterns return to their pre-pandemic, endemic dynamics and ana-  
<sup>14</sup> lyze time series data from Hong Kong, Canada, Korea, and the US from the resulting  
<sup>15</sup> framework. By quantifying the resilience of common respiratory pathogens, we are  
<sup>16</sup> able to predict when each pathogen will eventually return to their pre-pandemic, en-  
<sup>17</sup> demic dynamics. Our predictions about whether each pathogen should have already  
<sup>18</sup> returned to their pre-pandemic dynamics closely match the observed patterns of de-  
<sup>19</sup> viations (or lack thereof) from their pre-pandemic dynamics. Discrepancies between  
<sup>20</sup> predicted and observed dynamics indicate long-term impact of pandemic perturba-  
<sup>21</sup> tions, suggesting a possibility that some pathogens may have converged to a different  
<sup>22</sup> endemic cycle. Finally, we show that the replenishment rate of the susceptible pool is  
<sup>23</sup> a key determinant of pathogen resilience, which in turn determines the sensitivity of  
<sup>24</sup> a system to stochastic perturbations. Overall, our analysis highlight the persistence  
<sup>25</sup> of common respiratory pathogens.

Non-pharmaceutical interventions (NPIs) to slow the spread of SARS-CoV-2 disrupted the transmission of other human respiratory pathogens, adding uncertainties to their future epidemic dynamics and the overall public health burden [1]. As NPIs lifted, large heterogeneities in outbreak dynamics were observed across different pathogens in different countries, with some pathogens exhibiting earlier resurgences than others [2, 3, 4]. Heterogeneities in the overall reduction in transmission and the timing of re-emergence likely reflect differences in NPI patterns, pathogen characteristics, immigration/importation from other countries, and pre-pandemic pathogen dynamics [5]. Therefore, comparing the differential impact of the pandemic perturbations across pathogens can provide unique opportunities to learn about underlying pathogen characteristics, such as their transmissibility or duration of immunity, from heterogeneities in re-emergence patterns [6].

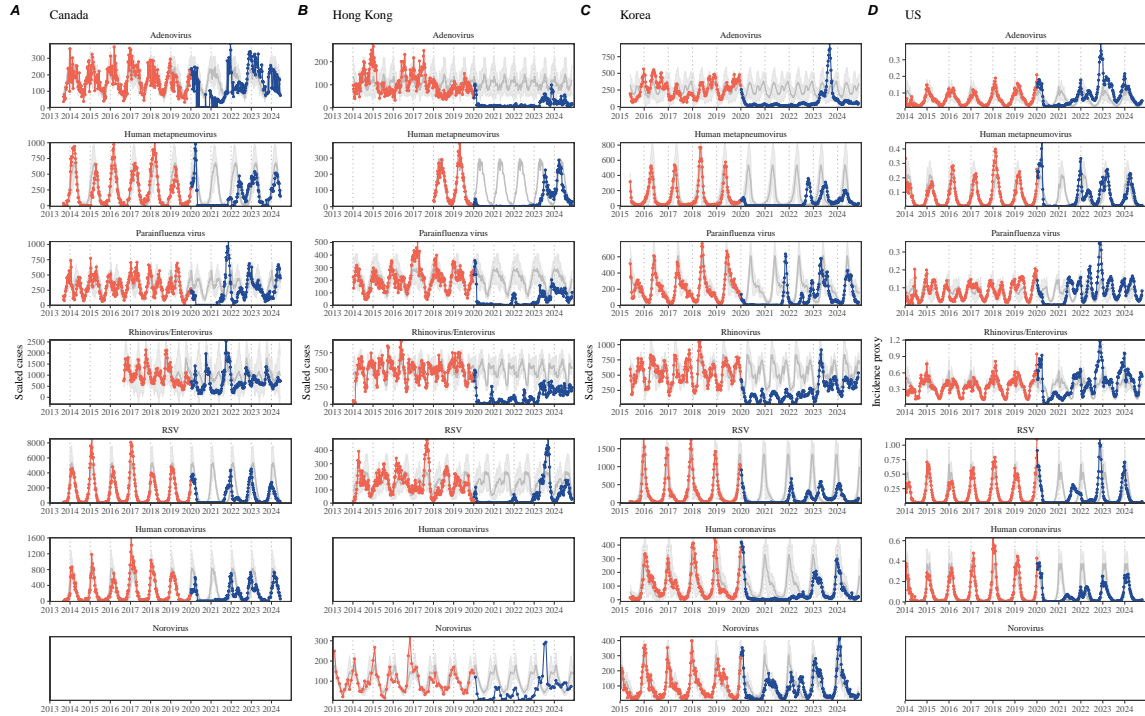


**Figure 1: Observed heterogeneity in responses to pandemic perturbations across respiratory pathogens and norovirus in (A) Canada, (B) Hong Kong, (C) Korea, and (D) US.** Red points and lines represent data before 2020. Blue points and lines represent data since 2020. Gray lines and shaded regions represent the mean seasonal patterns and corresponding 95% confidence intervals around the mean. Mean seasonal patterns were calculated by aggregating cases before 2020 into 52 weekly bins and taking the average in each week. Cases were scaled to account for changes in testing patterns (Materials and Methods).

Even though more than five years have passed since the emergence of SARS-CoV-2, we still observe persistent changes in pathogen dynamics following the pandemic

40 perturbations: for example, compared to pre-pandemic, seasonal patterns, human  
41 metapneumovirus in Korea seem to circulate at lower levels, whereas RSV in Ko-  
42 rea seem to exhibit different seasonality (Figure 1). These observations suggest a  
43 possibility for a fundamental change in pathogen dynamics following the pandemic  
44 perturbations, which can be driven by permanent shift in either human behavior  
45 or population-level immunity [7, 8]. The possibility of a long-lasting impact of the  
46 pandemic perturbations pose an important question for future infectious disease dy-  
47 namics: can we predict whether and when other respiratory pathogens will eventually  
48 return to their pre-pandemic dynamics? *[SWP: You suggested: I would say some-  
49 thing about the dynamics of these pathogens not being well understood, but I've  
50 since rewritten the most of intro and I'm not sure where I would fit this. If you have  
51 any suggestions, let me know...]*

52 So far, the majority of epidemiological analyses of respiratory pathogens in the  
53 context of the pandemic perturbations have focused on characterizing the timing of  
54 rebound [1, 9, 5]. Instead, we seek to characterize how fast a pathogen returns to its  
55 pre-pandemic dynamics. These two concepts have subtle but important differences:  
56 for example, it took more than 3 years for human metapneumovirus to rebound in  
57 Hong Kong but the observed epidemic patterns in 2024 are similar to pre-pandemic  
58 seasonal means, suggesting a rapid return to pre-pandemic dynamics following a  
59 perturbation (Figure 1). Measuring this rate of return is particularly useful because  
60 it allows us to quantify the ecological resilience of a host-pathogen system [10, 11,  
61 12, 13].

62 In this study, we lay out theoretical and statistical approaches to characterizing  
63 the resilience of a host-pathogen system based on how fast the system recovers from  
64 perturbation. We begin by laying out a few representative scenarios that capture  
65 the potential impact of pandemic perturbations on endemic pathogen dynamics and  
66 illustrate how resilience can be measured by comparing the pre- and post-pandemic  
67 dynamics of susceptible and infected hosts. In practice, information on susceptible  
68 hosts is often unavailable, making this theoretical approach infeasible. Instead, we  
69 utilize a mathematical technique to reconstruct empirical attractors from the data  
70 [14], which allows us to measure the rate at which the host-pathogen system ap-  
71 proaches this empirical attractor after a perturbation; this rate corresponds to the  
72 resilience of the host-pathogen system. We use this method to analyze pathogen  
73 surveillance data for respiratory and non-respiratory pathogens from Canada, Hong  
74 Kong, Korea, and US. Finally, we show that susceptible host dynamics explain vari-  
75 ation in pathogen resilience and further link pathogen resilience to responses to  
76 perturbations caused by demographic stochasticity, thereby providing a direct link  
77 between pathogen resilience and persistence.

## 78 Conceptual introduction to pathogen resilience

79 In classical ecological literature, resilience of an ecological system is measured by  
80 the rate at which the system returns to its reference state following a perturbation  
81 [10, 11, 12, 13]. This rate corresponds to the largest real part of the eigenvalues of  
82 the linearized system near equilibrium—here, we refer to this value as the *intrinsic*  
83 resilience of the system, which represents the expected rate of return from perturbed  
84 states. In practice, we rarely know the true model describing population-level dy-  
85 namics of common respiratory pathogens, limiting our ability to infer the intrinsic  
86 resilience of a system. Instead, we can still measure the *empirical* resilience of a  
87 host-pathogen system by looking at how fast the system returns to the pre-pandemic,  
88 endemic dynamics after interventions are lifted.

89 As an example, we begin with a simple Susceptible-Infected-Recovered-Susceptible  
90 (SIRS) model with seasonally forced transmission and demography (i.e., birth and  
91 death). The SIRS model is the simplest model that allows for waning of immunity  
92 and is commonly used for modeling the dynamics of respiratory pathogens [15]. First,  
93 consider an intervention that reduce transmission by 50% for 6 months starting in  
94 2020, which causes epidemic patterns to deviate from its original stable annual cycle  
95 for a short period of time and eventually come back (Figure 2A). To measure the  
96 resilience of this system empirically, we first need to be able to measure the dis-  
97 tance from its pre-pandemic attractor. There are many ways we can measure the  
98 distance from the attractor, but for illustrative purposes, we choose one of the most  
99 parsimonious approach: that is, we look at how the susceptible (S) and infected (I)  
100 populations change over time and measure the distance on the SI phase plane (Figure  
101 2B). In this simple case, the locally estimated scatterplot smoothing (LOESS) fit in-  
102 dicates that the distance from the attractor decreases exponentially (linearly on a log  
103 scale) on average (Figure 2C). Furthermore, the overall rate of return approximates  
104 the intrinsic resilience of the seasonally unforced system (Figure 2C).

105 Alternatively, pandemic perturbations can have a lasting impact on the pathogen  
106 dynamics; as an example, we consider a scenario in which a 10% reduction in trans-  
107 mission persists even after interventions are lifted (Figure 2D–F). In such cases in  
108 practice, we cannot know whether the pathogen will return to its original cycle or a  
109 different cycle until many years have passed, and we cannot measure the distance to  
110 the new unknown attractor that the system might eventually approach. Nonethe-  
111 less, we can still measure the distance from the pre-pandemic attractor and ask  
112 how the distance changes over time (Figure 2E). The LOESS fit suggests that the  
113 distance from the pre-pandemic attractor will initially decrease exponentially on av-  
114 erage (equivalently, linearly on a log scale) and eventually plateau (Figure 2F). Here,  
115 a permanent 10% reduction in transmission rate slows the system, which causes the  
116 distance from the pre-pandemic attractor initially to decrease at a slower rate (Figure  
117 2F) than it would have otherwise (Figure 2C) before plateauing at a fixed distance  
118 between the two attractors. This example shows that resilience is not necessarily an  
119 intrinsic property of a specific pathogen. Instead, pathogen resilience is a property

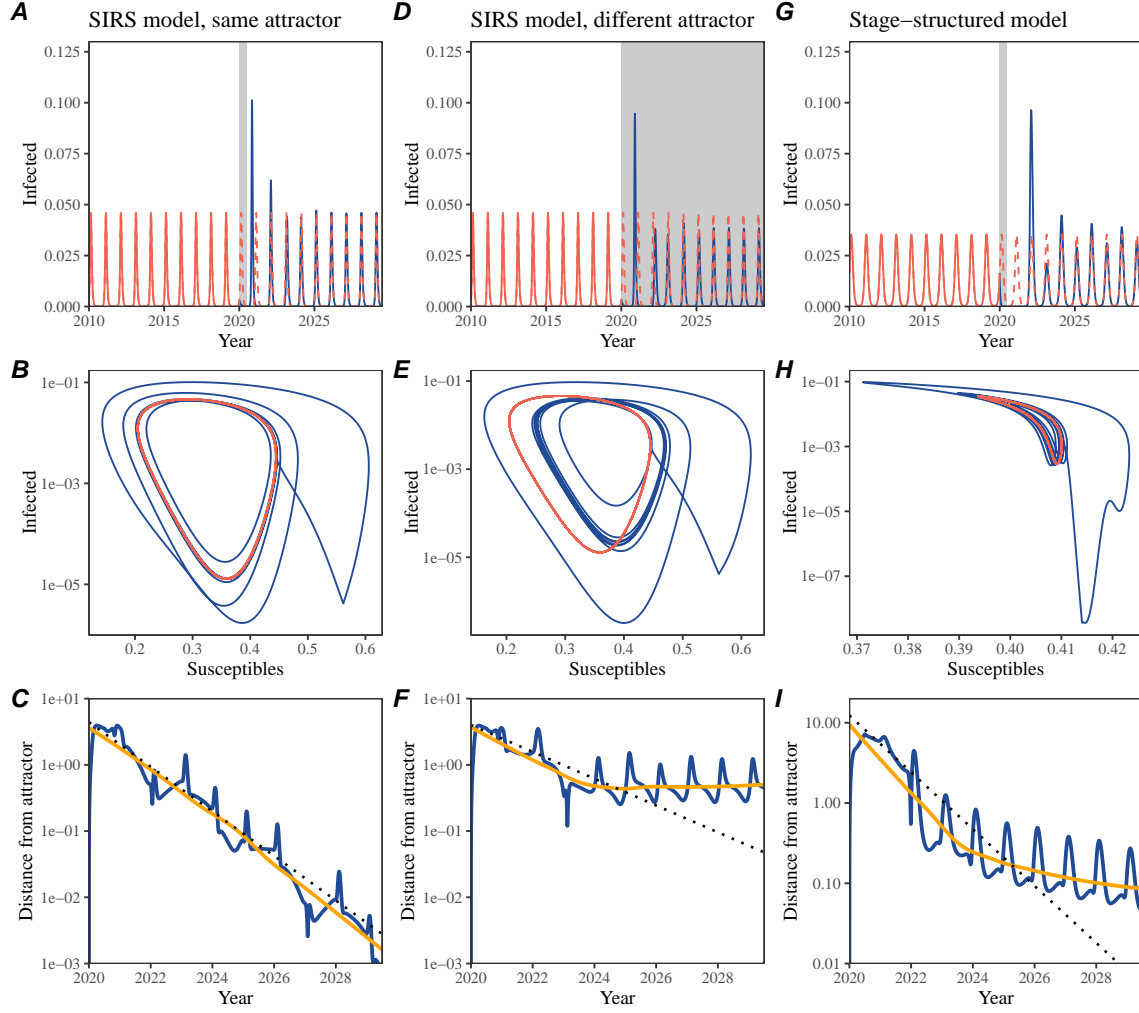


**Figure 2: A simple method to measure pathogen resilience following pandemic perturbations across different scenarios.** (A, D, G) Simulated epidemic trajectories across various models. Red and blue solid lines represent epidemic dynamics before and after interventions are introduced, respectively. Red dashed lines represent counterfactual epidemic dynamics in the absence of interventions. Gray regions indicate the duration of interventions. (B, E, H) Phase plane representation of the time series in panels A, D, and G alongside the corresponding susceptible host dynamics. Red and blue solid lines represent epidemic trajectories on an SI phase plane before and after interventions are introduced, respectively. (C, F, I) Changes in logged distance from the attractor over time. Blue lines represent the logged distance from the attractor. Orange lines represent the locally estimated scatterplot smoothing (LOESS) fits to the logged distance from the attractor. Dotted lines show the intrinsic resilience of the seasonally unforced system.

120 of a specific attractor that a host-pathogen system approaches, which depends on

121 both pathogen and host characteristics.

122 Finally, transient phenomena can further complicate the picture (Figure 2G–I).  
123 For example, a stage-structured model initially exhibits a stable annual cycle, but  
124 perturbations from a 10% reduction in transmission for 6 months cause the epidemic  
125 to shift to biennial cycles (Figure 2G). The system eventually approaches the original  
126 pre-pandemic attractor (Figure 2H), suggesting that this biennial cycle is a transient  
127 phenomenon. The LOESS fit indicates that the distance from the attractor initially  
128 decreases exponentially at a rate that is consistent with the intrinsic resilience of  
129 the seasonally unforced stage-structured system, but the rate of decrease decelerates  
130 with the damped oscillations (Figure 2I). This behavior is also referred to as a ghost  
131 attractor, which causes long transient dynamics and slow transitions [16]. Strong  
132 seasonal forcing in transmission can also lead to transient phenomena for a simple  
133 SIRS model, causing a slow return to pre-perturbation dynamics (Supplementary  
134 Figure S1).

135 This empirical approach allows us to measure the resilience of a two-strain host-  
136 pathogen system even when we have incomplete observation of the infection dynam-  
137 ics. Simulations from a simple two-strain system illustrate that separate analyses of  
138 individual strain dynamics (e.g., RSV A vs B) and a joint analysis of total infections  
139 (e.g., total RSV infections) yield identical resilience estimates (Supplementary Fig-  
140 ure S2, 3). This is expected because the dynamics of two strains (or two pathogens)  
141 around the attractor in a coupled system are described by the same set of eigen-  
142 values and eigenvectors, meaning that both strains should exhibit identical rates of  
143 returns following a perturbation. Analogous to a single system, strong seasonal forc-  
144 ing in transmission can cause the system to slow down through transient phenomena  
145 (Supplementary Figure S4).

146 These observations indicate three possibilities. First, we can directly estimate the  
147 empirical resilience of a host-pathogen system by measuring the rate at which the  
148 system approaches an attractor, provided that we have a way to quantify the distance  
149 from the attractor. The empirical approach to estimating pathogen resilience is  
150 particularly convenient because it does not require us to know the true underlying  
151 model; estimating the intrinsic resilience from fitting misspecified models can lead  
152 to biased estimates (Supplementary Figure S5). Second, resilience estimates allow  
153 us to make phenomenological predictions about the dynamics of a host-pathogen  
154 system following a perturbation. Assuming that the distance from the attractor will  
155 decrease exponentially over time, we can obtain a ballpark estimate for when the  
156 system will reach an attractor; this prediction necessarily assumes that there won't  
157 be permanent changes in pathogen dynamics (Figure 2F) or a long-term transient  
158 phenomenon (Figure 2I). Finally, a change in the rate of an exponential decrease in  
159 the distance from the attractor can provide information about whether the system  
160 has reached an alternative attractor, or a ghost attractor, that is different from the  
161 original, pre-pandemic attractor. These alternative attractors may reflect continued  
162 perturbations from permanent changes in transmission patterns as well as changes in  
163 immune landscapes. There will be periods of time when it is difficult to tell whether

164 pathogen dynamics are still diverging from its original attractor or have begun to  
165 converge to an attractor; now that several years have passed since interventions have  
166 been lifted, we expect many respiratory pathogens to have had sufficient time to  
167 begin returning to their post-intervention attractors.

## 168 Inferring pathogen resilience from real data

169 Based on these observations, we now lay out our approach to estimating pathogen  
170 resilience from real data (Figure 3). We then test this approach against simulations  
171 and apply it to real data.

172 So far, we focused on simple examples that assume a constant transmission re-  
173 duction. However, in practice, the impact of pandemic perturbations on pathogen  
174 transmission is likely more complex (Figure 3A), reflecting introduction and relax-  
175 ation of various intervention strategies. In some cases, strong perturbations can even  
176 lead to a local fadeout, requiring immigration from another location for epidemic re-  
177 emergence. These complexities can lead to longer delays between the introduction of  
178 pandemic perturbations and pathogen re-emergence as well as temporal variation in  
179 outbreak sizes (Figure 3B): in this example, continued transmission reduction from  
180 interventions limits the size of the first outbreak in 2021 following the emergence,  
181 allowing for a larger outbreak in 2022 when interventions are further relaxed.

182 Previously, we relied on the dynamics of susceptible and infected hosts to com-  
183 pute the distance from the attractor (Figure 2), but information on susceptible hosts  
184 is rarely available in practice. In addition, uncertainties in case counts due to obser-  
185 vation error as well as multiannual cycles in the observed epidemic dynamics (e.g.,  
186 adenovirus circulation patterns in Hong Kong and Korea) add challenges to defin-  
187 ing pre-pandemic attractors, which limits our ability to measure the distance from  
188 the attractor. To address these challenges, we can reconstruct an empirical attrac-  
189 tor by utilizing Takens' theorem [14], which states that an attractor of a nonlinear  
190 multidimensional system can be mapped onto a delayed embedding (Materials and  
191 Methods). For example, we can use delayed logged values of pre-pandemic cases  $C(t)$   
192 (Figure 3C) to reconstruct the attractor:

$$\langle \log(C(t) + 1), \log(C(t - \tau) + 1), \dots, \log(C(t - (M - 1)\tau) + 1) \rangle, \quad (1)$$

193 where the delay  $\tau$  and embedding dimension  $M$  are determined based on autocor-  
194 relations and false nearest neighbors, respectively [17, 18]. We can then apply the  
195 same delay and embedding dimensions to the entire time series to determine the  
196 position on a multi-dimensional state space (Figure 3D), which allows us to mea-  
197 sure the nearest neighbor distance between the current state of the system and the  
198 empirical pre-pandemic attractor (Figure 3E). In theory, we can now quantify how  
199 fast this distance decreases by fitting a linear regression on a log scale, where the  
200 slope of the linear regression corresponds to pathogen resilience. However, resulting  
201 estimates of pathogen resilience can be sensitive to choices about embedding delays

and dimensions; for example, using longer delays and higher dimensions tends to smooth out temporal variations in the distance from the attractor (Supplementary Figure S6).

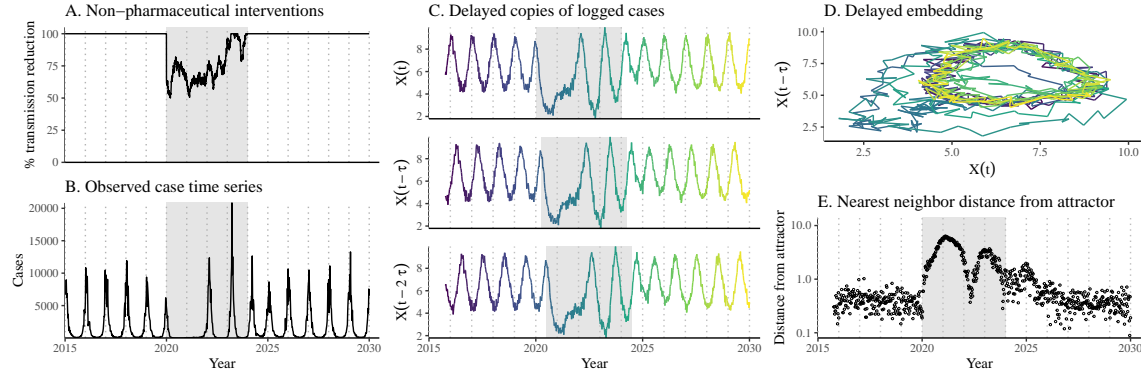


**Figure 3: A schematic diagram explaining the inference of pathogen resilience from synthetic data.** (A) A realistic example of simulated pandemic perturbations, represented by a relative reduction in transmission. (B) The impact of the synthetic pandemic perturbation on epidemic dynamics simulated using a SIRS model with demographic stochasticity. (C) Generating delayed copies of the logged time series allows us to obtain an embedding. (D) Two dimensional representation of an embedding. (E) Delayed embedding allows us to calculate the nearest neighbor distance from the empirical attractor, which is determined based on the pre-pandemic time series. This distance time series can be used to infer pathogen resilience after choosing an appropriate window for linear regression.

Complex changes in the distance from the attractor suggest that estimating pathogen resilience from linear regression will be particularly sensitive to our choice of fitting windows for the regression (Figure 3E). Therefore, before we tried estimating resilience from real data, we explored an automated window selection criterion for linear regression and test it against randomized, stochastic simulations across a wide range of realistic pandemic perturbation shapes; in doing so, we also explored optimal choices for embedding dimensions and evaluated our choices for fitting window parameters and embedding dimensions by quantifying correlation coefficients between the estimated resilience and the intrinsic resilience of a seasonally unforced system (Materials and Methods). Overall, we find large variation in estimation performances with correlation coefficient ranging from 0.21 to 0.61 (Supplementary Figure S7). In almost all cases, the automated window selection approach outperformed a naive approach that uses the entire time series, starting from the peak distance (Supplementary Figure S7).

Based on the best performing window selection criteria and embedding dimension, we applied this approach to pathogen surveillance data presented in Figure 1 (Materials and Methods). For each time series, we applied Takens' theorem independently to reconstruct the empirical attractor and obtained the corresponding

223 time series of distances from attractors (Supplementary Figure S8). Then, we use  
224 the automated window selection criterion to fit a linear regression and estimate the  
225 empirical resilience for each pathogen in each country (Supplementary Figure S8);  
226 the window selection criterion gave poor regression window for three cases (norovirus  
227 in Hong Kong and Korea and Rhinovirus/Enterovirus in the US), leading to unrealistically  
228 low resilience estimates, and so we used ad-hoc regression windows instead  
229 (Supplementary Figure S9; Materials and Methods).

230 For all pathogens we consider, resilience estimates fall between 0.4/year and  
231 1.8/year (Figure 4A). We estimate the mean resilience of common respiratory pathogens  
232 to be 0.99/year (95% CI: 0.81/year–1.18/year). As a reference, this is  $\approx$  7.5 times  
233 higher than the intrinsic resilience of pre-vaccination measles in England and Wales  
234 ( $\approx$  0.13/year). Finally, resilience estimates for norovirus are comparable to those of  
235 common respiratory pathogens: 1.44/year (95%CI: 1.01/year–1.87/year) for Hong  
236 Kong and 1.07/year (95%CI: 0.86/year–1.29/year) for Korea. Based on a simple  
237 ANOVA test, we do not find significant differences in resilience estimates across  
238 countries ( $p = 0.25$ ) or pathogens ( $p = 0.67$ ).

239 [SWP: You suggested “I think we probably need to spell out a bit more that  
240 long-term changes in the transmission rate (or some other parameter) mean the at-  
241 tractor is permanently different and the distance should remain nonzero” and I think  
242 we’ve done that enough early on with current revisions so I don’t feel like we need  
243 to do it again here. Let me know what you think.] Using resilience estimates, we  
244 predicted when each pathogen would hypothetically return to their pre-pandemic  
245 dynamics, assuming no long-term change in the attractor. Specifically, we extend  
246 our linear regression fits to distance-from-attractor time series and ask when the pre-  
247 dicted regression line will cross a threshold value; since we relied on nearest neighbor  
248 distances, pre-pandemic distances are always greater than zero (Figure 3E), meaning  
249 that we can use the mean of pre-pandemic distances as our threshold.

250 We predict that a return to pre-pandemic cycles would be imminent for most  
251 pathogens (Figure 4B). In particular, we predict that 12 out of 23 pathogens should  
252 have already returned before the end of 2024. For almost all pathogens that are  
253 predicted to have returned already, the observed epidemic dynamics show clear con-  
254 vergence towards their pre-pandemic seasonal averages, confirming our predictions  
255 (Figure 4C). However, there are a few exceptions, including norovirus in Hong Kong  
256 and Rhinovirus/Enterovirus in the US, where the observed epidemic dynamics in  
257 2024 exhibit clear deviation from their pre-pandemic seasonal averages (Figure 4C).  
258 These observations suggest a possibility that some common respiratory pathogens  
259 may have converged to different attractors or are still exhibiting non-equilibrium  
260 dynamics. In contrast, pathogens that are predicted to have not returned yet also  
261 show clear differences from their pre-pandemic seasonal averages; as many of these  
262 pathogens are predicted to return in 2025–2026, we may be able to test these pre-  
263 dictions in near future (Supplementary Figure S10). Our reconstructions of distance  
264 time series and estimates of pathogen resilience and expected return time are gener-  
265 ally robust to choices of embedding dimensions (Supplementary Figure S11–12).

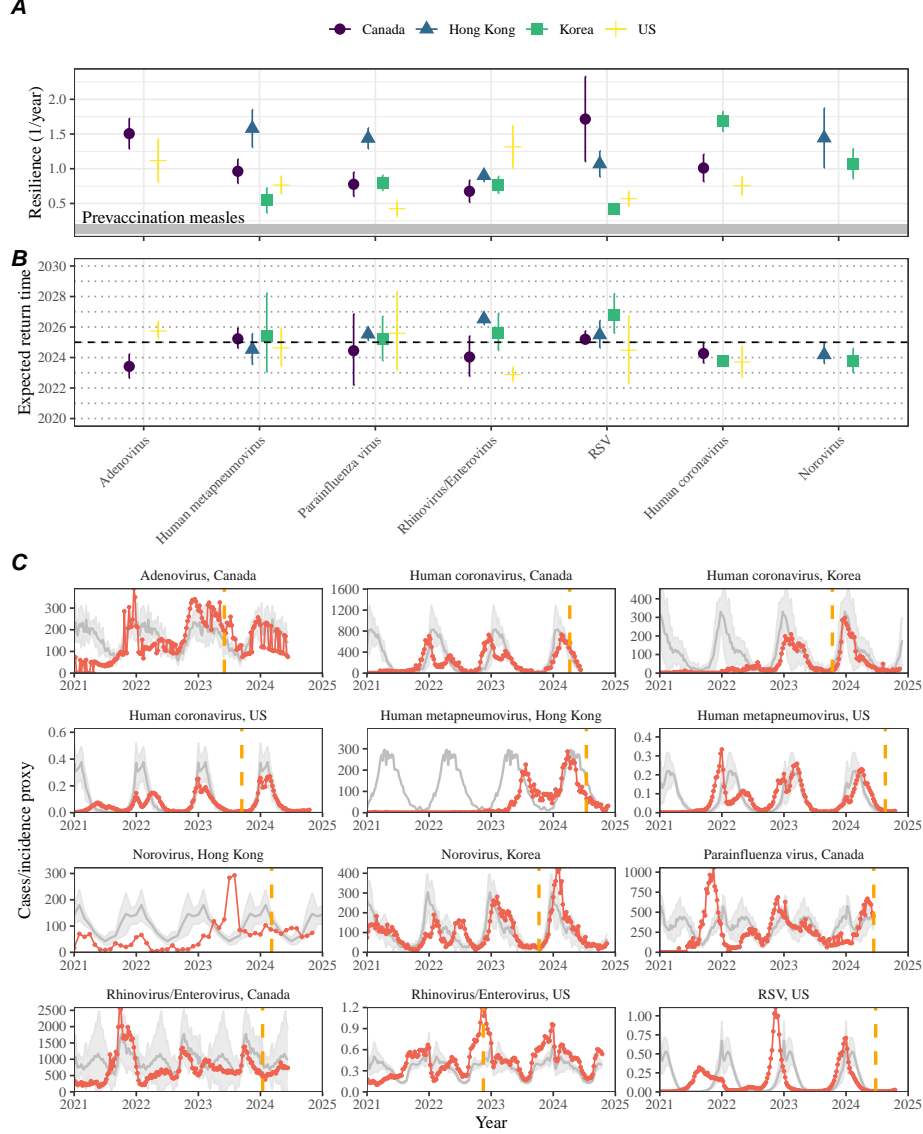


**Figure 4: Summary of resilience estimates and predictions for return time.** (A) Estimated pathogen resilience. The gray horizontal line represents the intrinsic resilience of pre-vaccination measles dynamics. (B) Predicted timing of when each pathogen will return to their pre-pandemic cycles. The dashed line in panel B indicates the end of 2024 (current observation time). Error bars represent 95% confidence intervals. (C) Observed dynamics for pathogen that are predicted to have returned before the end of 2024. Red points and lines represent data before 2020. Gray lines and shaded regions represent the mean seasonal patterns and corresponding 95% confidence intervals around the mean, previously shown in Figure 1. Orange vertical lines represent the predicted timing of return.

266 **Susceptible host dynamics explain variation in pathogen  
267 resilience**

268 So far, we focused on quantifying pathogen resilience from the observed patterns  
269 of pathogen re-emergence following pandemic perturbations. But what factors de-  
270 termine how resilient a host-pathogen system is? Here, we use the SIRS model to  
271 show that susceptible host dynamics are the key determinants of pathogen resilience.  
272 To do so, we vary the basic reproduction number  $\mathcal{R}_0$ , which represents the average  
273 number of secondary infections caused by a newly infected individual in a fully sus-  
274 ceptible population, and the duration of immunity and compute intrinsic resilience  
275 for each parameter.

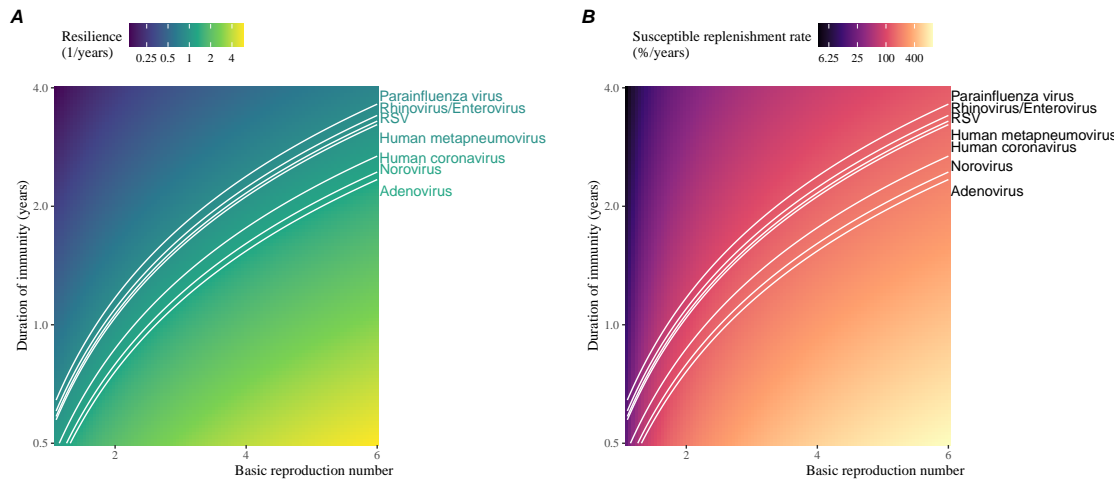


Figure 5: **Linking pathogen resilience to epidemiological parameters and susceptible host dynamics.** (A) The heat map represents intrinsic resilience as a function of the basic reproduction number  $\mathcal{R}_0$  and the duration of immunity. (B) The heat map represents per-capita susceptible replenishment rate as a function of the basic reproduction number  $\mathcal{R}_0$  and the duration of immunity. The standard SIRS model is used to compute intrinsic resilience and per-capita susceptible replenishment rate. Lines correspond to a set of parameters that are consistent with mean resilience estimates for each pathogen. Pathogens are ranked based on their mean resilience estimates, averaged across different countries.

276 We find an increase in  $\mathcal{R}_0$  and a decrease in duration of immunity correspond  
277 to an increase in pathogen resilience (Figure 5A). These variations can be under-  
278 stood in terms of the susceptible host dynamics, where faster per-capita susceptible  
279 replenishment rate causes the system to be more resilient (Figure 5B). This rate can  
280 be expressed as a ratio between absolute rate at which new susceptibles enter the  
281 population and the equilibrium number of susceptible individuals in the population,  
282  $\bar{S}$ . Therefore, both higher  $\mathcal{R}_0$  and shorter duration of immunity can drive faster

283 per-capita susceptible replenishment rate (Figure 5B), especially because higher  $\mathcal{R}_0$   
284 leads to lower  $\bar{S}$ .

285 We can also rank different pathogens based on the average values of empirical  
286 resilience computed previously, which allows us to determine a set of parameters that  
287 are consistent with the estimated resilience (Figure 5A). Across all pathogens we  
288 consider, except for bocavirus and norovirus, we estimate that the average duration  
289 of immunity is likely to be short (< 4 years) across a plausible range of  $\mathcal{R}_0$  (< 6).  
290 These rankings further allow us to map each pathogen onto a set of SIRS parameters  
291 that are consistent with its empirical resilience (Figure 5A) and obtain a plausible  
292 range of susceptible replenishment rates for each pathogen (Figure 5B). However, we  
293 note that there is no one-to-one correspondence between susceptible replenishment  
294 rates and pathogen resilience, leading to a wide uncertainty in the estimates for  
295 susceptible replenishment rates (Figure 5B).

## 296 **Pathogen resilience determines sensitivity to stochastic perturbations**

297

298 Beyond the pandemic perturbations, we expect host-pathogen systems to experience  
299 continued perturbations of varying degrees from changes in epidemiological conditions,  
300 such as human behavior, climate, and viral evolution. These perturbations  
301 can also arise from demographic stochasticity, which is inherent to any ecological  
302 systems. Here, we use a seasonally unforced SIRS model with birth/death to explore  
303 how resilience of a host-pathogen system determines the sensitivity to perturbations  
304 caused by demographic stochasticity (Materials and Methods).

305 We find that resilience of a host-pathogen system determines the amount of deviation  
306 from the deterministic trajectory caused by demographic stochasticity, with less  
307 resilient systems experiencing larger deviations (Figure 6). Notably, less resilience  
308 systems also exhibit slower epidemic cycles; the periodicity of this epidemic cycle  
309 matches those predicted by the intrinsic periodicity of the system (Supplementary  
310 Figure S13). These conclusions are robust for the seasonally forced SIRS model  
311 (Supplementary Figure S14),

## 312 **Discussion**

313 The pandemic interventions have caused major disruptions to circulation patterns of  
314 both respiratory and non-respiratory pathogens, adding challenges to predicting their  
315 future dynamics [1, 2, 3, 4]. However, these perturbations offer large-scale natural  
316 experiments for understanding how different pathogens respond to perturbations. In  
317 this study, we showed that pathogen re-emergence patterns following pandemic per-  
318 turbations can be characterized through the lens of ecological resilience. We showed  
319 that variation in pathogen resilience can be explained by the differences in suscepti-

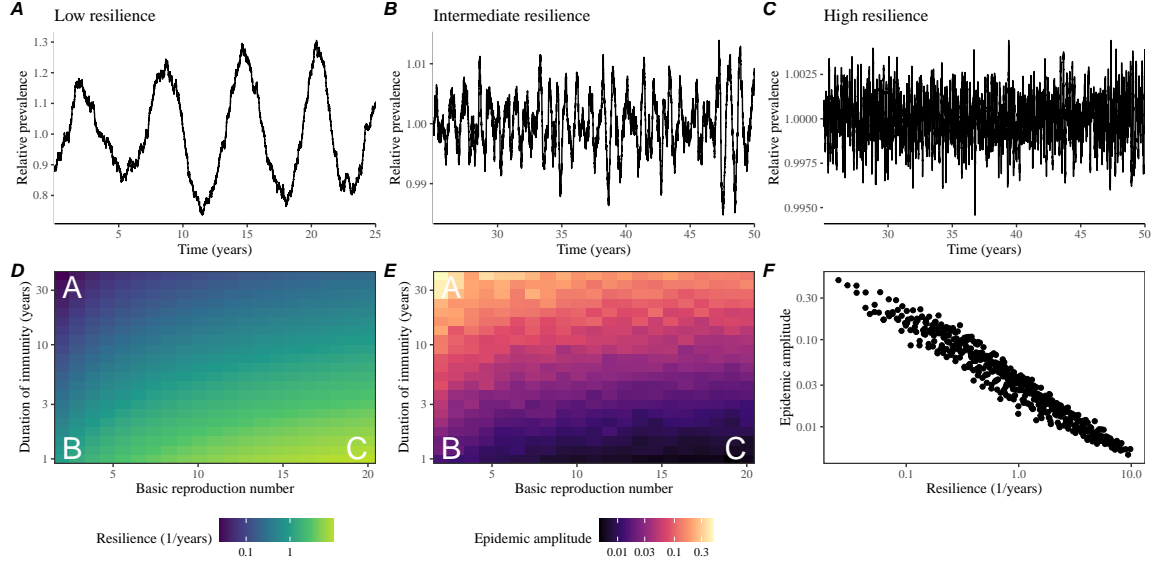


**Figure 6: Linking resilience of a host-pathogen system to its sensitivity to stochastic perturbations.** (A–C) Epidemic trajectories of a stochastic SIRS model across three different resilience values: low, intermediate, and high. The relative prevalence was calculated by dividing infection prevalence by its mean value. (D) The heat map represents the intrinsic resilience of a system as a function of the basic reproduction number  $\mathcal{R}_0$  and the duration of immunity. (E) The heat map represents the epidemic amplitude as a function of the basic reproduction number  $\mathcal{R}_0$  and the duration of immunity. The epidemic amplitude corresponds to  $(\max I - \min I)/(2\bar{I})$ , where  $\bar{I}$  represents the mean prevalence. (F) The relationship between pathogen resilience and epidemic amplitude.

320 ble host dynamics, where faster replenishment of the susceptible pool corresponds to  
 321 a more resilient host-pathogen system. Finally, we showed that pathogen resilience  
 322 also determines the sensitivity to stochastic perturbations.

323 We analyzed case time series of common respiratory infections and norovirus  
 324 infections from Canada, Hong Kong, Korea, and the US to estimate their resilience.  
 325 Overall, we estimated the resilience of these pathogens to range from 0.4/year to  
 326 1.8/year, which is 3–14 times more resilient than prevaccination measles. These  
 327 resilience estimates indicate that common respiratory pathogens and norovirus likely  
 328 exhibit faster susceptible replenishment and are therefore more persistent, indicating  
 329 potential challenges in controlling these pathogens.

330 Based on our resilience estimates, we made phenomenological predictions about  
 331 when each pathogen will return to their endemic cycles. For the most part, we  
 332 accurately predicted which pathogens should have already returned before the end  
 333 of 2024. However, there were few exceptions (i.e., norovirus in Hong Kong and  
 334 rhinovirus/enterovirus in the US), suggesting a possibility that these may have con-

335 verged to different endemic cycles compared to their pre-pandemic epidemic patterns.  
336 These changes may reflect changes in surveillance or actual shift in the dynamics,  
337 caused by permanent changes in behavior or population-level immunity. While it may  
338 seem unlikely that permanent changes in behavior would only affect a few pathogens  
339 and not others, we cannot rule out this possibility given heterogeneity in the age of  
340 infection across different respiratory pathogens [19, 20]. Differences in the mode of  
341 transmission between respiratory vs gastrointestinal pathogens may also contribute  
342 to the differences in responses to pandemic perturbations. However, it is unclear  
343 why norovirus dynamics in Korea seemed to have returned, whereas those in Hong  
344 Kong have not.

345 For almost half of the pathogens we considered, we predicted that their return  
346 to original epidemic patterns is imminent. We will need a few more years of data  
347 to test whether these pathogens will eventually return to their original dynamics  
348 or eventually converge to a different attractor. Overall, these observations echo  
349 earlier studies that highlighted the long-lasting impact of pandemic perturbations  
350 [8, 21, 22, 4].

351 We showed that susceptible host dynamics shape pathogen resilience, where faster  
352 replenishment of the susceptible population causes the pathogen to be more resilient.  
353 For simplicity, we focus on waning immunity and birth as the main drivers of the  
354 susceptible host dynamics but other mechanisms can also contribute to the replen-  
355 ishment of the susceptible population. In particular, pathogen evolution, especially  
356 the emergence of antigenically novel strains, can cause effective waning of immunity  
357 in the population; therefore, we hypothesize that faster rates of antigenic evolution  
358 can also cause a pathogen to be more resilient. Future studies should explore the  
359 relationship between the rate of evolution and resilience for antigenically evolving  
360 pathogens.

361 Quantifying pathogen resilience also offers novel approaches to validating population-  
362 level epidemiological models. So far, most of model validation in infectious disease  
363 ecology is based on the ability of a model to reproduce the observed epidemic dy-  
364 namics and to predict future dynamics [23, 24, 25, 26, 27]. However, many models  
365 can perform similarly under these criteria. For example, two major RSV models  
366 have been proposed to explain biennial epidemic patterns: (1) a stage- and age-  
367 structured model that allows disease severity to vary with number of past infections  
368 and age of infection [25] and (2) a pathogen-interaction model that accounts for cross  
369 immunity between RSV and human metapneumovirus [24]. Since both models can  
370 accurately reproduce the observed epidemic patterns, standard criteria for model  
371 validation do not allow us to distinguish between these two models from population-  
372 level data alone. Instead, it would be possible to measure the empirical resilience of  
373 each model by simulating various perturbations and compare them to estimates of  
374 empirical resilience from data, using pandemic NPIs as an opportunity.

375 There are several limitations to our work. First, we did not extensively explore  
376 other approaches to reconstructing the attractor. Recent studies showed that more  
377 sophisticated approaches, such as using non-uniform embedding, can provide more

robust reconstruction for noisy data [18]. In the context of causal inference, choices about embedding can have major impact on the resulting inference [28]. Our resilience estimates are likely overly confident given a lack of uncertainties in attractor reconstruction as well as the simplicity of our statistical framework. Nonetheless, as illustrated in our sensitivity analyses, inferences about pathogen resilience in our SIRS model appear to be robust to decisions about embedding lags and dimensions—this is because tracking the rate at which the system approaches the attractor is likely a much simpler problem than making inferences about causal directionality. Short pre-pandemic time series also limit our ability to accurately reconstruct the attractor and contribute to the crudeness of our resilience estimates; although this is less likely a problem for respiratory pathogens that are strongly annual, our attractor reconstruction may be inaccurate for those exhibiting multi-annual cycles, such as adenovirus in Hong Kong and Korea. Uncertainties in pathogen dynamics due to changes in testing patterns further contribute to the curdeness of our resilience estimates. Despite these limitations, our qualitative prediction that common respiratory pathogens are more resilient than prevaccination measles is also likely to be robust, given how rapid many respiratory pathogens returned to their original cycles following pandemic NPIs.

Predicting the impact of anthropogenic changes on infectious disease dynamics is a fundamental aim of infectious disease research in a rapidly changing world. Our study illustrates that how a host-pathogen system responds to both small and large perturbations is largely predictable through the lens of ecological resilience. In particular, quantifying the resilience of a host-pathogen system offers a unique insight into questions about endemic pathogens' responses to pandemic perturbations, including whether some pathogens will exhibit long-lasting impact from the pandemic perturbation or not. More broadly, a detailed understanding of the determinants of pathogen resilience can provide deeper understanding of pathogen persistence.

## Materials and Methods

### Data

We gathered time series on respiratory infections from Canada, Hong Kong, Korea, and United States (US). As a reference, we also included time series data on norovirus infections for available countries. In contrast to respiratory pathogens, we expect gastrointestinal viruses, such as norovirus, to be differently affected by pandemic perturbations.

Weekly time series of respiratory infection cases in Canada comes from a publicly available website by the Respiratory Virus Detection Surveillance System, which collect data from select laboratories across Canada [29]. Weekly time series of respiratory infection cases in Hong Kong comes from a publicly available website by the Centre for Health Protection, Department of Health [30, 31]. Weekly time series of acute respiratory infection cases in Korea comes from a publicly available website by

418 the Korea Disease Control and Prevention Agency [32]. Finally, weekly time series  
419 of respiratory infection cases in the US were obtained from the National Respiratory  
420 and Enteric Virus Surveillance System. Time series on number of tests were also  
421 available in Canada, Hong Kong, and the US, but not in Korea. **[SWP: Not sure**  
422 *how to cite NREVSS data because we got it by emailing them...*]

423 **Data processing**

424 For all time series, we rounded every year to 52 weeks by taking the average number  
425 of cases and tests between the 52nd and 53rd week. We also rescale all time series to  
426 account for changes in testing patterns, which are then used for the actual analysis.

427 For Canada, an increase in testing was observed from 2013 to 2024 (Supplemen-  
428 tary Figure S15). To account for this increase, we calculated a 2 year moving average  
429 for the number of tests for each pathogen, which we used as a proxy for testing effort.  
430 Then, we divided the smoothed testing patterns by the smoothed value at the final  
431 week such that the testing effort has a maximum of 1. We then divided weekly cases  
432 by the testing effort to obtain a scaled case time series. A similar approach was used  
433 earlier for an analysis of RSV time series in the US to account for changes in testing  
434 patterns [25].

435 For Hong Kong, we also applied the same scaling procedure to the time series  
436 as we did for Canada. In this case, we only adjusted for testing efforts up to the  
437 end of 2019 because there was a major reduction in testing for common respiratory  
438 pathogens since 2020 (Supplementary Figure S16).

439 For Korea, while we did not have information on testing, the reported number  
440 of respiratory infections consistently increased from 2013 to the end of 2019, which  
441 we interpreted as changes in testing patterns (Supplementary Figure S17). Since  
442 we did not have testing numbers, we used the weekly sum of all acute respiratory  
443 viral infection cases as a proxy for testing, which were further smoothed with moving  
444 averaged and scaled to have a maximum of 1. For Korea, we also only adjusted for  
445 testing efforts up to the end of 2019.

446 In the US, there has been a large increase in testing against some respiratory  
447 pathogens, especially RSV, which could not be corrected for through simple scaling  
448 (Supplementary Figure S18). Instead, we derived an incidence proxy by multiply-  
449 ing the test positivity with influenza-like illness positivity, which was taken from  
450 <https://gis.cdc.gov/grasp/fluview/fluportaldashboard.html>. This method  
451 of estimating an incidence proxy has been recently applied in the analysis of seasonal  
452 coronaviruses [7] and *Mycoplasma pneumoniae* infections [4]. Detailed assumptions  
453 and justifications are provided in [33].

454 **Estimating pathogen resilience**

455 In order to measure pathogen resilience from surveillance data, we first reconstructed  
456 the empirical pre-pandemic attractor of the system using Takens' embedding theorem

[14]. Specifically, for a given pathogen, we took the pre-pandemic (before 2020) case time series  $C(t)$  and reconstruct the attractor using delayed embedding with a uniform delay of  $\tau$  and dimension  $M$ :

$$X_{\tau,M}(t) = \langle \log(C(t) + 1), \log(C(t - \tau) + 1), \dots, \log(C(t - (M - 1)\tau) + 1) \rangle. \quad (2)$$

Here, the delay  $\tau$  was determined by calculating the autocorrelation of the logged pre-pandemic time series and asking when the autocorrelation crosses 0 for the first time [18]; a typical delay for an annual outbreak is around 13 weeks.

Then, for a given delay  $\tau$ , we determined the embedding dimension  $M$  using the false nearest neighbors approach [17, 18]. To do so, we started with an embedding dimension  $e$  and construct a set of points  $A_{\tau,e} = \{X_{\tau,e}(t) | t < 2020\}$ . Then, for each point  $X_{\tau,e}(t)$ , we determined the nearest neighbor from the set  $A_{\tau,e}$ , which we denote  $X_{\tau,e}(t_{nn})$  for  $t \neq t_{nn}$ . Then, if the distance between these two points on  $e + 1$  dimension,  $D_{\tau,e+1}(t) = \|X_{\tau,e+1}(t_{nn}) - X_{\tau,e+1}(t)\|_2$ , is larger than their distance on  $e$  dimension,  $D_{\tau,e}(t) = \|X_{\tau,e}(t_{nn}) - X_{\tau,e}(t)\|_2$ , these two points are deemed to be false nearest neighbors; specifically, we used a threshold  $R$  for the ratio between two distances  $D_{\tau,e+1}(t)/D_{\tau,e}(t)$  to determine false nearest neighbors. For the main analysis, we used  $R = 10$ , which was chosen from a sensitivity analysis against simulated data (Supplementary Text). Once we determined the embedding lag  $\tau$  and dimension  $M$ , we apply the embedding to the entire time series and calculate the nearest neighbor distance against the attractor  $A_{\tau,M}$  to obtain a time series of distance from the attractor  $D_{\tau,M}(t)$ .

From a time series of distances from the attractor, we estimated pathogen resilience by fitting a linear regression to an appropriate window. To automatically select the fitting window, we began by smoothing the distance time series using locally estimated scatterplot smoothing (LOESS) to obtain  $\hat{D}_{\tau,M}(t)$ , where the smoothing is performed on a log scale and exponentiated afterwards. Then, we determined threshold values ( $T_{\text{start}}$  and  $T_{\text{end}}$ ) for the smoothed distances and choose the fitting window based on when  $\hat{D}_{\tau,M}(t)$  crosses these threshold values for the first time. These thresholds were determined by first calculating maximum distance,

$$\max \hat{D} = \max \hat{D}_{\tau,M}(t), \quad (3)$$

and mean pre-pandemic distance,

$$\hat{D}_{\text{mean}} = \frac{1}{N_{t < 2020}} \sum_{t < 2020} \hat{D}_{\tau,M}(t), \quad (4)$$

as a reference, and then dividing their ratios into  $K$  equal bins:

$$T_{\text{start}} = \hat{D}_{\text{mean}} \times \left( \frac{\max \hat{D}}{\hat{D}_{\text{mean}}} \right)^{(K-a)/K} \quad (5)$$

$$T_{\text{end}} = \hat{D}_{\text{mean}} \times \left( \frac{\max \hat{D}}{\hat{D}_{\text{mean}}} \right)^{a/K} \quad (6)$$

487 where  $a$  represents the truncation threshold. This allows us to discard the initial  
 488 period during which the distance increases (from the introduction of intervention  
 489 measures) and the final period during which the distance plateaus (as the system  
 490 reaches an attractor). The fitting window is determined based on when the smoothed  
 491 distance  $\hat{D}_{\tau,M}(t)$  crosses these threshold values for the first time; then, we fit a  
 492 linear regression to logged (unsmoothed) distances  $\log D_{\tau,M}(t)$  using that window.  
 493 Alongside the threshold  $R$  for the false nearest neighbors approach, we tested optimal  
 494 choices for  $K$  and  $a$  values using simulations (Supplementary Text). We used  $K = 19$   
 495 and  $a = 2$  throughout the paper based on the simulation results.

## 496 Mathematical modeling

497 Throughout the paper, we use a series of mathematical models to illustrate the  
 498 concept of pathogen resilience and to understand the determinants of pathogen re-  
 499 silience. In general, the intrinsic resilience for a given system is given by the largest  
 500 real part of the eigenvalues of the linearized system at endemic equilibrium. Here, we  
 501 focus on the SIRS model with demography (birth and death) and present the details  
 502 of other models in Supplementary Text. The SIRS (Susceptible-Infected-Recovered-  
 503 Susceptible) model is the simplest model that allows for waning of immunity, where  
 504 recovered (immune) individuals are assumed to become fully susceptible after an  
 505 average of  $1/\delta$  time period. The dynamics of the SIRS model is described by the  
 506 following set of differential equations:

$$\frac{dS}{dt} = \mu - \beta(t)SI - \mu S + \delta R \quad (7)$$

$$\frac{dI}{dt} = \beta(t)SI - (\gamma + \mu)I \quad (8)$$

$$\frac{dR}{dt} = \gamma I - (\delta + \mu)R \quad (9)$$

(10)

507 where  $\mu$  represents the birth/death rate,  $\beta(t)$  represents the time-varying trans-  
 508 mission rate, and  $\gamma$  represents the recovery rate. The basic reproduction number  
 509  $\mathcal{R}_0(t) = \beta(t)/(\gamma + \mu)$  is defined as the average number of secondary infections that  
 510 a single infected individual would cause in a fully susceptible population at time  $t$   
 511 and measures the intrinsic transmissibility of a pathogen.

512 When we first introduced the idea of pathogen resilience (Figure 2), we imposed  
 513 sinusoidal changes to the transmission rate to account for seasonal transmission:

$$\beta(t) = b_1(1 + \theta \cos(2\pi(t - \phi)))\alpha(t), \quad (11)$$

514 where  $b_1$  represents the baseline transmission rate,  $\theta$  represents the seasonal ampli-  
 515 tude, and  $\phi$  represents the seasonal offset term. Here, we also introduced an extra  
 516 multiplicative term  $\alpha(t)$  to account for the impact of pandemic perturbations, where

517  $\alpha(t) < 1$  indicates transmission reduction. Figure 2A and 2B were generated assuming  
 518  $b_1 = 3 \times (365/7 + 1/50)/\text{years}$ ,  $\theta = 0.2$ ,  $\phi = 0$ ,  $\mu = 1/50/\text{years}$ ,  $\gamma = 365/7/\text{years}$ ,  
 519 and  $\delta = 1/2/\text{years}$ , In Figure 2A, we imposed a 50% transmission reduction for 6  
 520 months from 2020:

$$\alpha(t) = \begin{cases} 0.5 & 2020 \leq t < 2020.5 \\ 1 & \text{otherwise} \end{cases} \quad (12)$$

521 In Figure 2B, we imposed a 50% transmission reduction for 6 months from 2020 and  
 522 a permanent 10% reduction onward:

$$\alpha(t) = \begin{cases} 1 & t < 2020 \\ 0.5 & 2020 \leq t < 2020.5 \\ 0.9 & 2020.5 \leq t \end{cases} \quad (13)$$

523 In both scenarios, we simulated the SIRS model from the following initial conditions  
 524 ( $S(0) = 1/\mathcal{R}_0$ ,  $I(0) = 1 \times 10^{-6}$ , and  $R(0) = 1 - S(0) - I(0)$ ) from 1900 until 2030.

525 To measure the empirical resilience of the SIRS model (Figure 2C and 2F), we  
 526 computed the normalized distance between post-intervention susceptible and logged  
 527 infected proportions and their corresponding unperturbed values at the same time:

$$\sqrt{\left(\frac{S(t) - S_{\text{unperturbed}}(t)}{\sigma_S}\right)^2 + \left(\frac{\log I(t) - \log I_{\text{unperturbed}}(t)}{\sigma_{\log I}}\right)^2}, \quad (14)$$

528 where  $\sigma_S$  and  $\sigma_{\log I}$  represent the standard deviation in the unperturbed susceptible  
 529 and logged infected proportions. The unperturbed values were obtained by simulating  
 530 the same SIRS model without pandemic perturbations ( $\alpha = 1$ ). We normalized  
 531 the differences in susceptible and logged infected proportions to allow both quantities  
 532 to equally contribute to the changes in distance from the attractor. We used logged  
 533 prevalence, instead of absolute prevalence, in order to capture epidemic dynamics  
 534 in deep troughs during the intervention period. In Supplementary Materials, we  
 535 also compared how the degree of seasonal transmission affects empirical resilience  
 536 by varying  $\theta$  from 0 to 0.4; when we assumed no seasonality ( $\theta = 0$ ), we did not  
 537 normalize the distance because the standard deviation of pre-intervention dynamics  
 538 are zero.

539 We used the SIRS model to understand how underlying epidemiological parameters  
 540 affect pathogen resilience and link this relationship to underlying susceptible  
 541 host dynamics. For the simple SIRS model without seasonal transmission ( $\theta = 0$ ),  
 542 the intrinsic resilience corresponds to

$$-\frac{\text{Re}(\lambda)}{2} = \frac{\delta + \beta I^* + \mu}{2}. \quad (15)$$

543 Here,  $I^*$  represents the prevalence at endemic equilibrium:

$$I^* = \frac{(\delta + \mu)(\beta - (\gamma + \mu))}{\beta(\delta + \gamma + \mu)}. \quad (16)$$

<sup>544</sup> The susceptible replenishment rate is given by

$$S_{\text{replenish}} = \frac{\mu + \delta R}{S^*}, \quad (17)$$

<sup>545</sup> where  $S^* = 1/\mathcal{R}_0$  represents the equilibrium proportion of susceptible individuals.  
<sup>546</sup> We varied the basic reproduction number  $\mathcal{R}_0$  between 1.1 to 6 and the average  
<sup>547</sup> duration of immunity  $1/\delta$  between 2 to 4 years, and computed these two quantities.  
<sup>548</sup> In doing so, we fixed all other parameters:  $\mu = 1/80/\text{years}$  and  $\gamma = 365/7/\text{years}$ .

<sup>549</sup> Finally, we used a seasonally unforced stochastic SIRS model without demog-  
<sup>550</sup> raphy to understand how pathogen resilience affects sensitivity of the system to  
<sup>551</sup> demographic stochasticity (see Supplementary Text for the details of the stochastic  
<sup>552</sup> SIRS model). By varying the basic reproduction number  $\mathcal{R}_0$  between 2 to 20 and  
<sup>553</sup> the average duration of immunity  $1/\delta$  between 1 to 40 years, we ran the the SIRS  
<sup>554</sup> model for 100 years and computed the epidemic amplitude, which we defined as  
<sup>555</sup>  $(\max I - \min I)/(2\bar{I})$ . Each simulation began from the equilibrium, and we trun-  
<sup>556</sup> cated initial 25 years before computing the epidemic amplitude. In doing so, we  
<sup>557</sup> assumed  $\gamma = 365/7/\text{years}$  and fixed the population size to 1 billion to prevent any  
<sup>558</sup> fadeouts. We also considered using a seasonally forced stochastic SIRS model with-  
<sup>559</sup> out demography, assuming an amplitude of seasonal forcing of 0.04; in this case,  
<sup>560</sup> we computed the relative epidemic amplitude by comparing the deterministic and  
<sup>561</sup> stochastic trajectories (Supplementary Materials).

## <sup>562</sup> Data availability

<sup>563</sup> All data and code are stored in a publicly available GitHub repository (<https://github.com/cobeylab/return-time>).  
<sup>564</sup>

## <sup>565</sup> Funding

<sup>566</sup> S.W.P. is a Peter and Carmen Lucia Buck Foundation Awardee of the Life Sciences  
<sup>567</sup> Research Foundation.

568 **Supplementary Text**

569 **Resilience of a stage-structured system.**

570 In Figure 2G–I, we used a more realistic, stage-structured model to illustrate how  
 571 transient phenomena can cause the system to slow down. Specifically, we used the  
 572 stage-structured RSV model proposed by [25], which assumes that subsequent rein-  
 573 fections cause an individual to become less susceptible and transmissible than previ-  
 574 ous infections. The model dynamics can be described as follows:

$$\frac{dM}{dt} = \mu - (\omega + \mu)M \quad (S1)$$

$$\frac{dS_0}{dt} = \omega M - (\lambda(t) + \mu)S_0 \quad (S2)$$

$$\frac{dI_1}{dt} = \lambda(t)S_0 - (\gamma_1 + \mu)I_1 \quad (S3)$$

$$\frac{dS_1}{dt} = \gamma_1 I_1 - (\sigma_1 \lambda(t) + \mu)S_1 \quad (S4)$$

$$\frac{dI_2}{dt} = \sigma_1 \lambda(t)S_1 - (\gamma_2 + \mu)I_2 \quad (S5)$$

$$\frac{dS_2}{dt} = \gamma_2 I_2 - (\sigma_2 \lambda(t) + \mu)S_2 \quad (S6)$$

$$\frac{dI_3}{dt} = \sigma_2 \lambda(t)S_2 - (\gamma_3 + \mu)I_3 \quad (S7)$$

$$\frac{dS_3}{dt} = \gamma_3 I_3 - (\sigma_3 \lambda(t) + \mu)S_3 + \gamma_4 I_4 \quad (S8)$$

$$\frac{dI_4}{dt} = \sigma_3 \lambda(t)S_3 - (\gamma_4 + \mu)I_4 \quad (S9)$$

(S10)

575 where  $M$  represents the proportion of individuals who are maternally immune;  $S_i$   
 576 represents the proportion of individuals who are susceptible after  $i$  prior infections;  $I_i$   
 577 represents the proportion of individuals who are currently (re)-infected with their  $i$ -th  
 578 infection;  $\mu$  represents the birth and death rates;  $1/\omega$  represents the mean duration  
 579 of maternal immunity;  $1/\gamma_i$  represents the mean duration of infection;  $\lambda(t)$  represents  
 580 the force of infection; and  $\sigma_i$  represents the reduction in susceptibility for the  $i$ -th  
 581 reinfection. The force of infection is modeled using a sinusoidal function:

$$\beta(t) = b_1(1 + \theta \cos(2\pi(t - \phi)))\alpha(t) \quad (S11)$$

$$\lambda(t) = \beta(I_1 + \rho_1 I_2 + \rho_2(I_3 + I_4)), \quad (S12)$$

582 where  $b_1$  represents the baseline transmission rate;  $\theta$  represents the seasonal ampli-  
 583 tude;  $\phi$  represents the seasonal offset term;  $\alpha(t)$  represents the intervention effect;  
 584 and  $\rho_i$  represents the impact of immunity on transmission reduction. We used the

585 following parameters to simulate the impact of interventions on epidemic dynam-  
 586 ics [25]:  $b_1 = 9 \times (365/10 + 1/80)/\text{years}$ ,  $\theta = 0.2$ ,  $\phi = -0.1$ ,  $\omega = 365/112/\text{years}$ ,  
 587  $\gamma_1 = 365/10/\text{years}$ ,  $\gamma_2 = 365/7/\text{years}$ ,  $\gamma_3 = 365/5/\text{years}$ ,  $\sigma_1 = 0.76$ ,  $\sigma_2 = 0.6$ ,  
 588  $\sigma_3 = 0.4$ ,  $\rho_1 = 0.75$ ,  $\rho_2 = 0.51$ , and  $\mu = 1/80/\text{years}$ . We assumed a 50% transmis-  
 589 sion reduction for 6 months from 2020:

$$\alpha(t) = \begin{cases} 0.5 & 2020 \leq t < 2020.5 \\ 1 & \text{otherwise} \end{cases} \quad (\text{S13})$$

590 The model was simulated from 1900 to 2030 using the following initial conditions:  
 591  $M = 0$ ,  $S_0 = 1/\mathcal{R}_0 - I_1$ ,  $I_1 = 1 \times 10^{-6}$ ,  $S_1 = 1 - 1/\mathcal{R}_0$ ,  $I_2 = 0$ ,  $S_2 = 0$ ,  $I_3 = 0$ ,  
 592  $S_3 = 0$ , and  $I_4 = 0$ . For the phase plane analysis (Figure 2H) and distance analysis  
 593 (Figure 2I), we relied on the average susceptibility,

$$\bar{S} = S_0 + \sigma_1 S_1 + \sigma_2 S_2 + \sigma_3 S_3, \quad (\text{S14})$$

594 and total prevalence,

$$I_{\text{total}} = I_1 + I_2 + I_3 + I_4. \quad (\text{S15})$$

595 These quantities were used to compute the normalized distance from the attractor,  
 596 as described in the main text.

## 597 Resilience of a multistrain system.

598 We used a simple two-strain model to show that a multistrain host-pathogen system  
 599 that is coupled through cross immunity can be described by a single resilience value.  
 600 The model dynamics can be described as follows [24]:

$$\frac{dS}{dt} = \mu - \mu S - (\lambda_1 + \lambda_2)S + \rho_1 R_1 + \rho_2 R_2 \quad (\text{S16})$$

$$\frac{dI_1}{dt} = \lambda_1 S - (\gamma_1 + \mu)I_1 \quad (\text{S17})$$

$$\frac{dI_2}{dt} = \lambda_2 S - (\gamma_2 + \mu)I_2 \quad (\text{S18})$$

$$\frac{dR_1}{dt} = \gamma_1 I_1 - \lambda_2 \epsilon_{21} R_1 - \rho_1 R_1 + \rho_2 R - \mu R_1 \quad (\text{S19})$$

$$\frac{dR_2}{dt} = \gamma_2 I_2 - \lambda_1 \epsilon_{12} R_2 - \rho_2 R_2 + \rho_1 R - \mu R_2 \quad (\text{S20})$$

$$\frac{dJ_1}{dt} = \lambda_1 \epsilon_{12} R_2 - (\gamma_1 + \mu)J_1 \quad (\text{S21})$$

$$\frac{dJ_2}{dt} = \lambda_2 \epsilon_{21} R_1 - (\gamma_2 + \mu)J_2 \quad (\text{S22})$$

$$\frac{dR}{dt} = \gamma_1 J_1 + \gamma_2 J_2 - \rho_1 R - \rho_2 R - \mu R \quad (\text{S23})$$

where  $S$  represents the proportion of individuals who are fully susceptible to infections by both strains;  $I_1$  represents the proportion of individuals who are infected with strain 1 without prior immunity;  $I_2$  represents the proportion of individuals who are infected with strain 2 without prior immunity;  $R_1$  represents the proportion of individuals who are fully immune against strain 1 and partially susceptible to reinfection by strain 2;  $R_2$  represents the proportion of individuals who are fully immune against strain 2 and partially susceptible to reinfection by strain 1;  $J_1$  represents the proportion of individuals who are infected with strain 1 with prior immunity against strain 2;  $J_2$  represents the proportion of individuals who are infected with strain 2 with prior immunity against strain 1;  $R$  represents the proportion of individuals who are immune to infections from both strains;  $\mu$  represents the birth/death rate;  $\lambda_1$  and  $\lambda_2$  represent the force of infection from strains 1 and 2, respectively;  $\rho_1$  and  $\rho_2$  represent the waning immunity rate;  $\gamma_1$  and  $\gamma_2$  represent the recovery rate;  $\epsilon_{12}$  and  $\epsilon_{21}$  represent the susceptibility to reinfection with strains 2 and 1, respectively, given prior immunity from infection with strains 1 and 2, respectively. The force of infection is modeled as follows:

$$\beta_1 = b_1(1 + \theta_1 \sin(2\pi(t - \phi_1)))\alpha(t) \quad (\text{S24})$$

$$\beta_2 = b_2(1 + \theta_2 \sin(2\pi(t - \phi_2)))\alpha(t) \quad (\text{S25})$$

$$\lambda_1 = \beta_1(I_1 + J_1) \quad (\text{S26})$$

$$\lambda_2 = \beta_2(I_2 + J_2) \quad (\text{S27})$$

In Supplementary Figures S2–S4, we assumed the following parameters:  $b_1 = 2 \times 52/\text{years}$ ,  $b_2 = 4 \times 52/\text{years}$ ,  $\phi_1 = \phi_2 = 0$ ,  $\epsilon_{12} = 0.9$ ,  $\epsilon_{21} = 0.5$ ,  $\gamma_1 = \gamma_2 = 52/\text{years}$ ,  $\rho_1 = \rho_2 = 1/\text{years}$ , and  $\mu = 1/70/\text{years}$ . For all simulations, we assumed a 50% transmission reduction for 6 months from 2020:

$$\alpha(t) = \begin{cases} 0.5 & 2020 \leq t < 2020.5 \\ 1 & \text{otherwise} \end{cases} \quad (\text{S28})$$

The seasonal amplitude  $\theta$  is varied from 0 to 0.4. All simulations were ran from 1900 to 2030 with following initial conditions:  $S(0) = 1 - 2 \times 10^{-6}$ ,  $I_1(0) = 1 \times 10^{-6}$ ,  $I_2(0) = 1 \times 10^{-6}$ ,  $R_1(0) = 0$ ,  $R_2(0) = 0$ ,  $J_1(0) = 0$ ,  $J_2(0) = 0$ , and  $R(0) = 0$ .

We considered three scenarios for measuring pathogen resilience: (1) we only have information about strain 1, (2) we only have information about strain 2, and (3) we are unable to distinguish between strains. In the first two scenarios (see panels A–C for strain 1 and panels D–F for strain 2), we considered the dynamics of average susceptibility for each strain and total prevalence:

$$\bar{S}_1 = S + \epsilon_{12}R_2 \quad (\text{S29})$$

$$\hat{I}_1 = I_1 + J_1 \quad (\text{S30})$$

$$\bar{S}_2 = S + \epsilon_{21}R_1 \quad (\text{S31})$$

$$\hat{I}_2 = I_2 + J_2 \quad (\text{S32})$$

629 In the third scenario (panels G–I), we considered the dynamics of total susceptible  
630 and infected populations:

$$\hat{S} = S + R_2 + R_1 \quad (\text{S33})$$

$$\hat{I} = I_1 + J_1 + I_2 + J_2 \quad (\text{S34})$$

631 These quantities were used to compute the normalized distance from the attractor,  
632 as described in the main text.

### 633 Estimating intrinsic resilience using mechanistic model

634 We tested whether we can reliably estimate the intrinsic resilience of a system by fit-  
635 ting a mechanistic model. Specifically, we simulated case time series from stochastic  
636 SIRS and two-strain models and fitted a simple, deterministic SIRS model using a  
637 Bayesian framework.

638 We simulated the models in discrete time with a daily time step ( $\Delta t = 1$ ),  
639 incorporating demographic stochasticity:

$$\beta(t) = \mathcal{R}_0 \left( 1 + \theta \cos \left( \frac{2\pi t}{364} \right) \right) \alpha(t)(1 - \exp(-\gamma)) \quad (\text{S35})$$

$$\text{FOI}(t) = \beta(t)I(t - \Delta t)/N \quad (\text{S36})$$

$$B(t) \sim \text{Poisson}(\mu N) \quad (\text{S37})$$

$$\Delta S(t) \sim \text{Binom}(S(t - \Delta t), 1 - \exp(-(\text{FOI}(t) + \mu)\Delta t)) \quad (\text{S38})$$

$$N_{SI}(t) \sim \text{Binom}\left(\Delta S(t), \frac{\text{FOI}(t)}{\text{FOI}(t) + \mu}\right) \quad (\text{S39})$$

$$\Delta I(t) \sim \text{Binom}(I(t - \Delta t), 1 - \exp(-(\gamma + \mu)\Delta t)) \quad (\text{S40})$$

$$N_{IR}(t) \sim \text{Binom}\left(\Delta I(t), \frac{\gamma}{\gamma + \mu}\right) \quad (\text{S41})$$

$$\Delta R(t) \sim \text{Binom}(R(t - \Delta t), 1 - \exp(-(\delta + \mu)\Delta t)) \quad (\text{S42})$$

$$N_{RS}(t) \sim \text{Binom}\left(\Delta R(t), \frac{\delta}{\delta + \mu}\right) \quad (\text{S43})$$

$$S(t) = S(t - \Delta t) + N_{RS}(t) + B(t) - \Delta S(t) \quad (\text{S44})$$

$$I(t) = I(t - \Delta t) + N_{SI}(t) - \Delta I(t) \quad (\text{S45})$$

$$R(t) = R(t - \Delta t) + N_{IR}(t) - \Delta R(t) \quad (\text{S46})$$

640 where FOI represent the force of infection;  $N_{ij}$  represent the number of individuals  
641 moving from compartment  $i$  to  $j$  on a given day; and  $B(t)$  represents the number  
642 of new births. We simulated the model on a daily scale—assuming 364 days in a  
643 year so that it can be evenly grouped into 52 weeks—with the following parameters:  
644  $\mathcal{R}_0 = 3$ ,  $\theta = 0.1$ ,  $\gamma = 1/7/\text{days}$ ,  $\delta = 1/(364 \times 2)/\text{days}$ ,  $\mu = 1/(364 \times 50)/\text{days}$ , and  
645  $N = 1 \times 10^8$ . The model was simulated from 1900 to 2030 assuming  $S(0) = N/3$ ,

<sup>646</sup>  $I(0) = 100$ , and  $R(0) = N - S(0) - I(0)$ . The observed incidence from the model  
<sup>647</sup> was then simulated as follows:

$$C(t) = \text{Beta-Binom}(N_{SI}(t), \rho, k), \quad (\text{S47})$$

<sup>648</sup> where  $\rho$  represents the reporting probability and  $k$  represents the overdispersion  
<sup>649</sup> parameter of beta-binomial distribution. Here, we used the beta-binomial distribution  
<sup>650</sup> to account for overdispersion in reporting. We assumed  $\rho = 0.002$  (i.e., 0.2%  
<sup>651</sup> probability) and  $k = 1000$ .

<sup>652</sup> We used an analogous approach for the two-strain model:

$$\beta_1(t) = b_1 \left( 1 + \theta_1 \cos \left( \frac{2\pi(t - \phi_1)}{364} \right) \right) \alpha(t) \quad (\text{S48})$$

$$\beta_2(t) = b_2 \left( 1 + \theta_2 \cos \left( \frac{2\pi(t - \phi_2)}{364} \right) \right) \alpha(t) \quad (\text{S49})$$

$$\text{FOI}_1(t) = \beta_1(t)(I_1(t - \Delta t) + J_1(t - \Delta t))/N \quad (\text{S50})$$

$$\text{FOI}_2(t) = \beta_2(t)(I_2(t - \Delta t) + J_2(t - \Delta t))/N \quad (\text{S51})$$

$$B(t) \sim \text{Poisson}(\mu N) \quad (\text{S52})$$

$$\Delta S(t) \sim \text{Binom}(S(t - \Delta t), 1 - \exp(-(\text{FOI}_1(t) + \text{FOI}_2(t) + \mu)\Delta t)) \quad (\text{S53})$$

$$N_{SI_1}(t) \sim \text{Binom}\left(\Delta S(t), \frac{\text{FOI}_1(t)}{\text{FOI}_1(t) + \text{FOI}_2(t) + \mu}\right) \quad (\text{S54})$$

$$N_{SI_2}(t) \sim \text{Binom}\left(\Delta S(t), \frac{\text{FOI}_2(t)}{\text{FOI}_1(t) + \text{FOI}_2(t) + \mu}\right) \quad (\text{S55})$$

$$\Delta I_1(t) \sim \text{Binom}(I_1(t - \Delta t), 1 - \exp(-(\gamma_1 + \mu)\Delta t)) \quad (\text{S56})$$

$$N_{I_1 R_1}(t) \sim \text{Binom}\left(\Delta I_1(t), \frac{\gamma_1}{\gamma_1 + \mu}\right) \quad (\text{S57})$$

$$\Delta I_2(t) \sim \text{Binom}(I_2(t - \Delta t), 1 - \exp(-(\gamma_2 + \mu)\Delta t)) \quad (\text{S58})$$

$$N_{I_2 R_2}(t) \sim \text{Binom}\left(\Delta I_2(t), \frac{\gamma_2}{\gamma_2 + \mu}\right) \quad (\text{S59})$$

$$\Delta R_1(t) \sim \text{Binom}(R_1(t - \Delta t), 1 - \exp(-(\epsilon_{21}\text{FOI}_2(t) + \rho_1 + \mu)\Delta t)) \quad (\text{S60})$$

$$N_{R_1 S}(t) \sim \text{Binom}\left(\Delta R_1(t), \frac{\rho_1}{\epsilon_{21}\text{FOI}_2(t) + \rho_1 + \mu}\right) \quad (\text{S61})$$

$$N_{R_1 J_2}(t) \sim \text{Binom}\left(\Delta R_1(t), \frac{\epsilon_{21}\text{FOI}_2(t)}{\epsilon_{21}\text{FOI}_2(t) + \rho_1 + \mu}\right) \quad (\text{S62})$$

$$\Delta R_2(t) \sim \text{Binom}(R_2(t - \Delta t), 1 - \exp(-(\epsilon_{12}\text{FOI}_1(t) + \rho_2 + \mu)\Delta t)) \quad (\text{S63})$$

$$N_{R_2 S}(t) \sim \text{Binom}\left(\Delta R_2(t), \frac{\rho_2}{\epsilon_{12}\text{FOI}_1(t) + \rho_2 + \mu}\right) \quad (\text{S64})$$

$$N_{R_2 J_1}(t) \sim \text{Binom}\left(\Delta R_2(t), \frac{\epsilon_{12}\text{FOI}_1(t)}{\epsilon_{12}\text{FOI}_1(t) + \rho_2 + \mu}\right) \quad (\text{S65})$$

$$\Delta J_1(t) \sim \text{Binom}(J_1(t - \Delta t), 1 - \exp(-(\gamma_1 + \mu)\Delta t)) \quad (\text{S66})$$

$$N_{J_1R}(t) \sim \text{Binom}\left(\Delta J_1(t), \frac{\gamma_1}{\gamma_1 + \mu}\right) \quad (\text{S67})$$

$$\Delta J_2(t) \sim \text{Binom}(J_2(t - \Delta t), 1 - \exp(-(\gamma_2 + \mu)\Delta t)) \quad (\text{S68})$$

$$N_{J_2R}(t) \sim \text{Binom}\left(\Delta J_2(t), \frac{\gamma_2}{\gamma_2 + \mu}\right) \quad (\text{S69})$$

$$\Delta R(t) \sim \text{Binom}(R(t - \Delta t), 1 - \exp(-(\rho_1 + \rho_2 + \mu)\Delta t)) \quad (\text{S70})$$

$$N_{RR_1}(t) \sim \text{Binom}\left(\Delta R(t), \frac{\rho_1}{\rho_1 + \rho_2 + \mu}\right) \quad (\text{S71})$$

$$N_{RR_2}(t) \sim \text{Binom}\left(\Delta R(t), \frac{\rho_2}{\rho_1 + \rho_2 + \mu}\right) \quad (\text{S72})$$

$$S(t) = S(t - \Delta t) - \Delta S(t) + B(t) + N_{R_1S}(t) + N_{R_2S}(t) \quad (\text{S73})$$

$$I_1(t) = I_1(t - \Delta t) - \Delta I_1(t) + N_{SI_1}(t) \quad (\text{S74})$$

$$I_2(t) = I_2(t - \Delta t) - \Delta I_2(t) + N_{SI_2}(t) \quad (\text{S75})$$

$$R_1(t) = R_1(t - \Delta t) - \Delta R_1(t) + N_{I_1R_1}(t) + N_{RR_1}(t) \quad (\text{S76})$$

$$R_2(t) = R_2(t - \Delta t) - \Delta R_2(t) + N_{I_2R_2}(t) + N_{RR_2}(t) \quad (\text{S77})$$

$$J_1(t) = J_1(t - \Delta t) - \Delta J_1(t) + N_{R_2J_1}(t) \quad (\text{S78})$$

$$J_2(t) = J_2(t - \Delta t) - \Delta J_2(t) + N_{R_1J_2}(t) \quad (\text{S79})$$

$$R(t) = R(t - \Delta t) - \Delta R(t) + N_{J_1R}(t) + N_{J_2R}(t) \quad (\text{S80})$$

We simulated the model on a daily scale with previously estimated parameters for the RSV-HMPV interaction [24]:  $b_1 = 1.7/\text{weeks}$ ,  $b_2 = 1.95/\text{weeks}$ ,  $\theta_1 = 0.4$ ,  $\theta_2 = 0.3$ ,  $\phi_1 = 0.005 \times 7/364$ ,  $\phi_2 = 4.99 \times 7/364$ ,  $\epsilon_{12} = 0.92$ ,  $\epsilon_{21} = 0.45$ ,  $\gamma_1 = 1/10/\text{days}$ ,  $\gamma_2 = 1/10/\text{days}$ ,  $\rho_1 = 1/364/\text{days}$ ,  $\rho_2 = 1/364/\text{days}$ ,  $\mu = 1/(70 \times 364)/\text{days}$ , and  $N = 1 \times 10^8$ . The model was simulated from 1900 to 2030 assuming  $S(0) = N - 200$ ,  $I_1(0) = 100$ ,  $I_2(0) = 100$ ,  $R_1(0) = 0$ ,  $R_2(0) = 0$ ,  $J_1(0) = 0$ ,  $J_2(0) = 0$ , and  $R(0) = 0$ . The observed incidence for each strain is then simulated as follows:

$$C_1(t) = \text{Beta-Binom}(N_{SI_1}(t) + N_{R_2J_1}, \rho, k), \quad (\text{S81})$$

$$C_2(t) = \text{Beta-Binom}(N_{SI_2}(t) + N_{R_1J_2}, \rho, k), \quad (\text{S82})$$

where  $\rho$  represents the reporting probability and  $k$  represents the overdispersion parameter of beta-binomial distribution. We assumed  $\rho = 0.002$  (i.e., 0.2% probability) and  $k = 500$ . We also considered the total incidence:  $C_{\text{total}}(t) = C_1(t) + C_2(t)$ .

For both models, we considered a more realistically shaped pandemic perturbation  $\alpha(t)$  to challenge our ability to estimate the intervention effects. Thus, we assumed a 40% transmission reduction for 3 months from March 2020, followed by a 10% transmission reduction for 6 months, 20% transmission reduction for 3 months,

667 and a final return to normal levels:

$$\alpha(t) = \begin{cases} 1 & t < 2020.25 \\ 0.6 & 2020.25 \leq t < 2020.5 \\ 0.9 & 2020.5 \leq t < 2021 \\ 0.8 & 2021 \leq t < 2021.25 \\ 1 & 2021.25 \leq t \end{cases}. \quad (\text{S83})$$

668 For all simulations, we truncated the time series from the beginning of 2014 to the  
669 end of 2023 and aggregate them into weekly cases.

670 To infer intrinsic resilience from time series, we fitted a simple discrete time,  
671 deterministic SIRS model [4]:

$$\Delta t = 1 \text{ week} \quad (\text{S84})$$

$$\text{FOI}(t) = \beta(t)(I(t - \Delta t) + \omega)/N \quad (\text{S85})$$

$$\Delta S(t) = [1 - \exp(-(\text{FOI}(t) + \mu)\Delta t)] S(t - \Delta t) \quad (\text{S86})$$

$$N_{SI}(t) = \frac{\text{FOI}(t)\Delta S(t)}{\text{FOI}(t) + \mu} \quad (\text{S87})$$

$$\Delta I(t) = [1 - \exp(-(\gamma + \mu)\Delta t)] I(t - \Delta t) \quad (\text{S88})$$

$$N_{IR}(t) = \frac{\gamma \Delta I(t)}{\gamma + \mu} \quad (\text{S89})$$

$$\Delta R(t) = [1 - \exp(-(\nu + \mu)\Delta t)] R(t - \Delta t) \quad (\text{S90})$$

$$N_{RS}(t) = \frac{\nu \Delta R(t)}{\nu + \mu} \quad (\text{S91})$$

$$S(t) = S(t - \Delta t) + \mu S - \Delta S(t) + N_{RS}(t) \quad (\text{S92})$$

$$I(t) = I(t - \Delta t) - \Delta I(t) + N_{SI}(t) \quad (\text{S93})$$

$$R(t) = R(t - \Delta t) - \Delta R(t) + N_{IR}(t) \quad (\text{S94})$$

672 where we include an extra term  $\omega$  to account for external infections. Although actual  
673 simulations did not include any external infections, we found that including this term  
674 generally helped with model convergence in previous analyses [4]. The transmission  
675 rate was divided into a seasonal term  $\beta_{\text{seas}}(t)$  (repeated every year) and intervention  
676 term  $\alpha(t)$ , which were estimated jointly:

$$\beta(t) = \beta_{\text{seas}}(t)\alpha(t), \quad (\text{S95})$$

677 where  $\alpha < 1$  corresponds to reduction in transmission due to intervention effects. To  
678 constrain the smoothness of  $\beta_{\text{seas}}(t)$ , we imposed cyclic, random-walk priors:

$$\beta_{\text{seas}}(t) \sim \text{Normal}(\beta_{\text{seas}}(t - 1), \sigma) \quad t = 2 \dots 52 \quad (\text{S96})$$

$$\beta_{\text{seas}}(1) \sim \text{Normal}(\beta_{\text{seas}}(52), \sigma) \quad (\text{S97})$$

679 [SWP: I noticed that I forgot to put a prior on  $\sigma$  so need to re-do this but won't  
 680 change the results.] We fixed  $\alpha(t) = 1$  for all  $t < 2020$  and estimate  $\alpha$  assuming a  
 681 normal prior:

$$\alpha \sim \text{Normal}(1, 0.25). \quad (\text{S98})$$

682 We assumed weakly informative priors on  $\omega$  and  $\nu$ :

$$\omega \sim \text{Normal}(0, 200) \quad (\text{S99})$$

$$\nu \sim \text{Normal}(104, 26) \quad (\text{S100})$$

683 We assumed that the true birth/death rates, population sizes, and recovery rates are  
 684 known. We note, however, that assuming  $\gamma = 1/\text{week}$  actually corresponds to a mean  
 685 simulated infectious period of 1.6 weeks, which is much longer than the true value;  
 686 this approximation allows us to test whether we can still robustly estimate the in-  
 687 trinsic resilience given parameter mis-specification. Initial conditions were estimated  
 688 with following priors:

$$S(0) = Ns(0) \quad (\text{S101})$$

$$I(0) = Ni(0) \quad (\text{S102})$$

$$s(0) \sim \text{Uniform}(0, 1) \quad (\text{S103})$$

$$i(0) \sim \text{Half-Normal}(0, 0.001) \quad (\text{S104})$$

689 Finally, the observation model was specified as follows:

$$\text{Cases}(t) \sim \text{Negative-Binomial}(\rho N_{SI}(t), \phi) \quad (\text{S105})$$

$$\rho \sim \text{Half-Normal}(0, 0.02) \quad (\text{S106})$$

$$\phi \sim \text{Half-Normal}(0, 10) \quad (\text{S107})$$

690 where  $\rho$  represents the reporting probability and  $\phi$  represents the negative binomial  
 691 overdispersion parameter.

692 The model was fitted to four separate time series: (1) incidence time series from  
 693 the SIRS model, (2) incidence time series for strain 1 from the two-strain model,  
 694 (3) incidence time series for strain 2 from the two-strain model, and (4) combined  
 695 incidence time series for strains 1 and 2 from the two-strain model. The model was  
 696 fitted using rstan [34, 35]. The resulting posterior distribution was used to calculate  
 697 the intrinsic resilience of the seasonally unforced system with the same parameters;  
 698 eigenvalues of the discrete-time SIR model were computed by numerically finding  
 699 the equilibrium and calculating the Jacobian matrix.

## 700 **Validations for window-selection criteria**

701 We used stochastic SIRS simulations to identify optimal parameters for the window-  
 702 selection criteria that we used for the linear regression for estimating empirical re-  
 703 silience. For each simulation, we began by generating a random perturbation  $\alpha(t)$

704 from a random set of parameters. First, we drew the duration of intervention  $\tau_{\text{npi}}$   
 705 from a uniform distribution between 1 and 2 years. Then, we drew independent  
 706 normal variables  $z_i$  of length  $\lfloor 364\tau_{\text{npi}} \rfloor$  with a standard deviation of 0.02 and took a  
 707 reverse cumulative sum to obtain a realistic shape for the intervention:

$$x_n = 1 + \sum_{i=n}^{\lfloor 364\tau_{\text{npi}} \rfloor} z_i, \quad n = 1, \dots, \lfloor 364\tau_{\text{npi}} \rfloor. \quad (\text{S108})$$

708 We repeated this random generation process until less than 10% of  $x_n$  exceeds 1—  
 709 this was done to prevent the perturbation  $\alpha(t)$  stays below 1 (and therefore reduce  
 710 transmission) for the most part. Then, we set any values that are above 1 or below 0  
 711 as 1 and 0, respectively. Then, we randomly drew the minimum transmission during  
 712 intervention  $\alpha_{\min}$  from a uniform distribution between 0.5 and 0.7 and scale  $x_n$  to  
 713 have a minimum of  $\alpha_{\min}$ :

$$x_{\text{scale},n} = \alpha_{\min} + (1 - \alpha_{\min}) \times \frac{x_n - \min x_n}{1 - \min x_n}. \quad (\text{S109})$$

714 This allowed us to simulate a realistically shaped intervention:

$$\alpha(t) = \begin{cases} 1 & t < 2020 \\ x_{\text{scale},364(t-2020)} & 2020 \leq t < 2020 + \tau_{\text{npi}} \\ 1 & \tau_{\text{npi}} \leq t \end{cases}. \quad (\text{S110})$$

715 Given this intervention function, we draw  $\mathcal{R}_0$  from a uniform distribution between 1.5  
 716 and 4 and the mean duration of immunity  $1/\delta$  from a uniform distribution between  
 717 1 and 4. Then, we simulate the stochastic SIRS model from  $S(0) = 10^8/\mathcal{R}_0$  and  
 718  $I(0) = 100$  from 1990 to 2025 and truncate the time series to 2014–2025; if the  
 719 epidemic becomes extinct before the end of simulation, we discard that simulation  
 720 and start over from the intervention generation step.

721 For each epidemic simulation, we computed the empirical resilience by varying  
 722 the threshold  $R$  for the nearest neighbor approach from 4 to 14 with increments of  
 723 2, the number of divisions  $K$  for the window selection between 8 and 25, and the  
 724 truncation threshold  $a$  for the window selection between 1 to 3; this was done for all  
 725 possible combinations of  $R$ ,  $K$ , and  $a$ . We also compared this with the naive approach  
 726 that uses the entire distance-from-attractor time series, starting from the maximum  
 727 distance to the end of the time series. We repeated this procedure 500 times and  
 728 quantified the correlation between empirical and intrinsic resilience estimates across  
 729 two approaches.

## Supplementary Figures

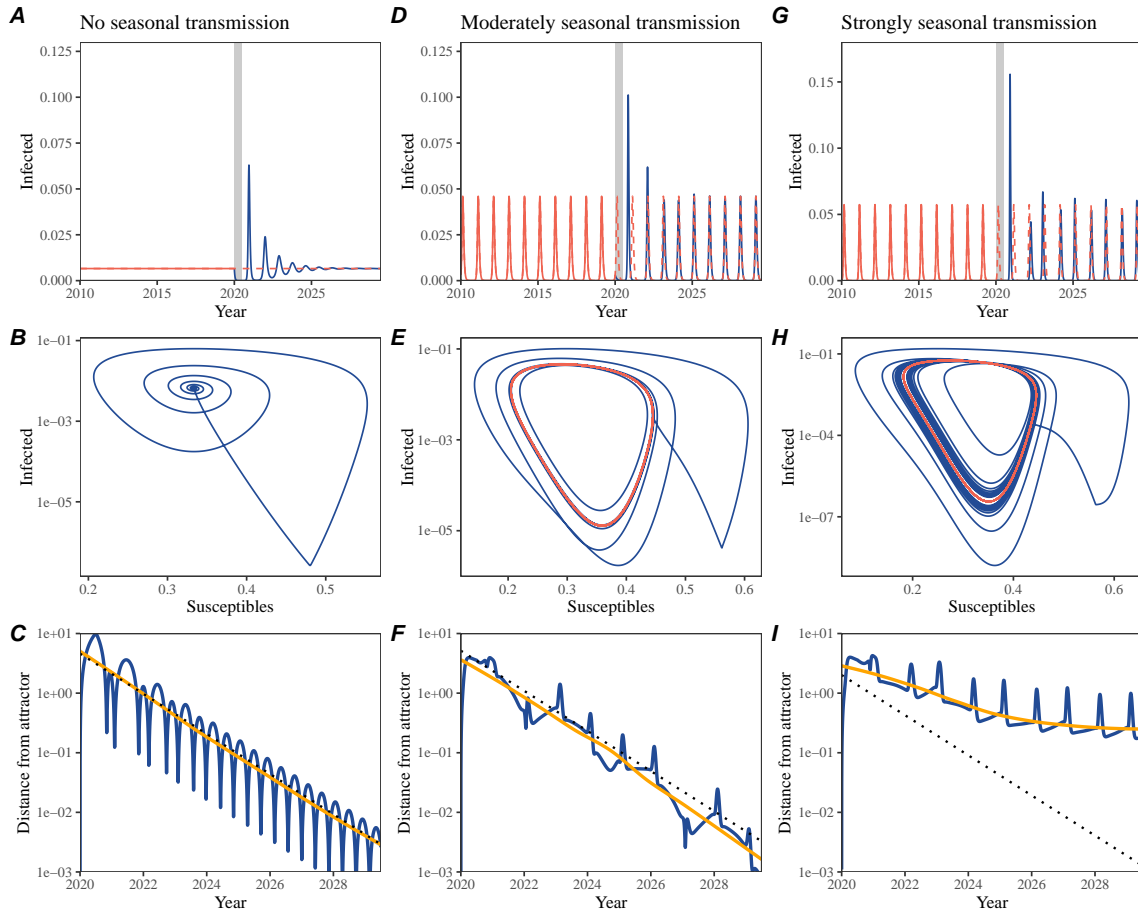


**Figure S1: Impact of seasonal transmission on pathogen resilience.** (A, D, G) Simulated epidemic trajectories using the SIRS model without seasonal forcing (A), with seasonal forcing of amplitude of 0.2 (D), and with seasonal forcing of amplitude of 0.4 (G). Red and blue solid lines represent epidemic dynamics before and after interventions are introduced, respectively. Red dashed lines represent counterfactual epidemic dynamics in the absence of interventions. Gray regions indicate the duration of interventions. (B, E, H) Phase plane representation of the time series in panels A, D, and G alongside the corresponding susceptible host dynamics. Red and blue solid lines represent epidemic trajectories on an SI phase plane before and after interventions are introduced, respectively. (C, F, I) Changes in logged distance from the attractor over time. Blue lines represent the logged distance from the attractor. Orange lines represent the locally estimated scatterplot smoothing (LOESS) fits to the logged distance from the attractor. Dotted lines show the intrinsic resilience of the seasonally unforced system.

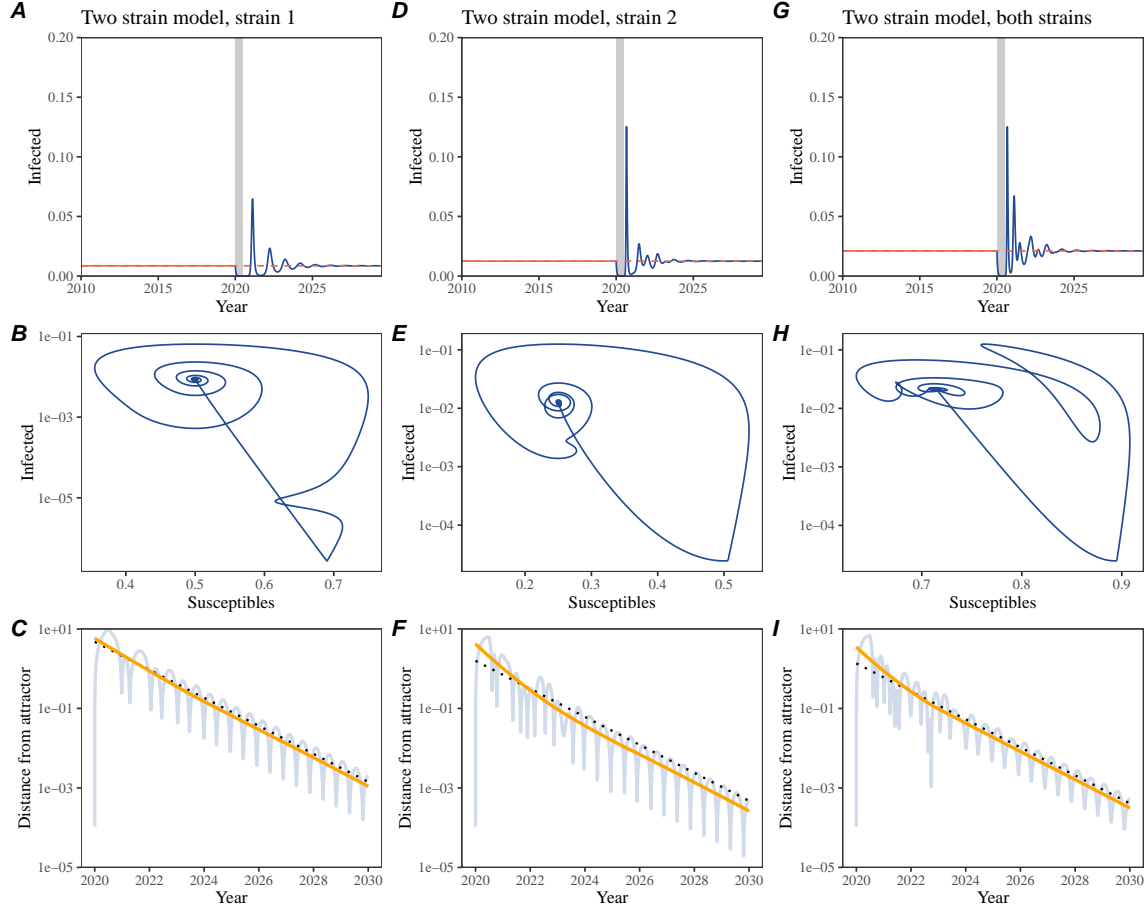


**Figure S2: Conceptual framework for measuring pathogen resilience following NPIs for a two-strain system without seasonal forcing.** (A, D, G) Simulated epidemic trajectories using a multi-strain system without seasonal forcing. Red and blue solid lines represent epidemic dynamics before and after interventions are introduced, respectively. Red dashed lines represent counterfactual epidemic dynamics in the absence of interventions. Gray regions indicate the duration of interventions. (B, E, H) Phase plane representation of the time series in panels A, D, and G alongside the corresponding susceptible host dynamics. Blue solid lines represent epidemic trajectories on an SI phase plane before and after interventions are introduced, respectively. (C, F, I) Changes in logged distance from the attractor over time. Blue lines represent the logged distance from the attractor. Orange lines represent the locally estimated scatterplot smoothing (LOESS) fits to the logged distance from the attractor. Dotted lines show the intrinsic resilience of the seasonally unforced system.

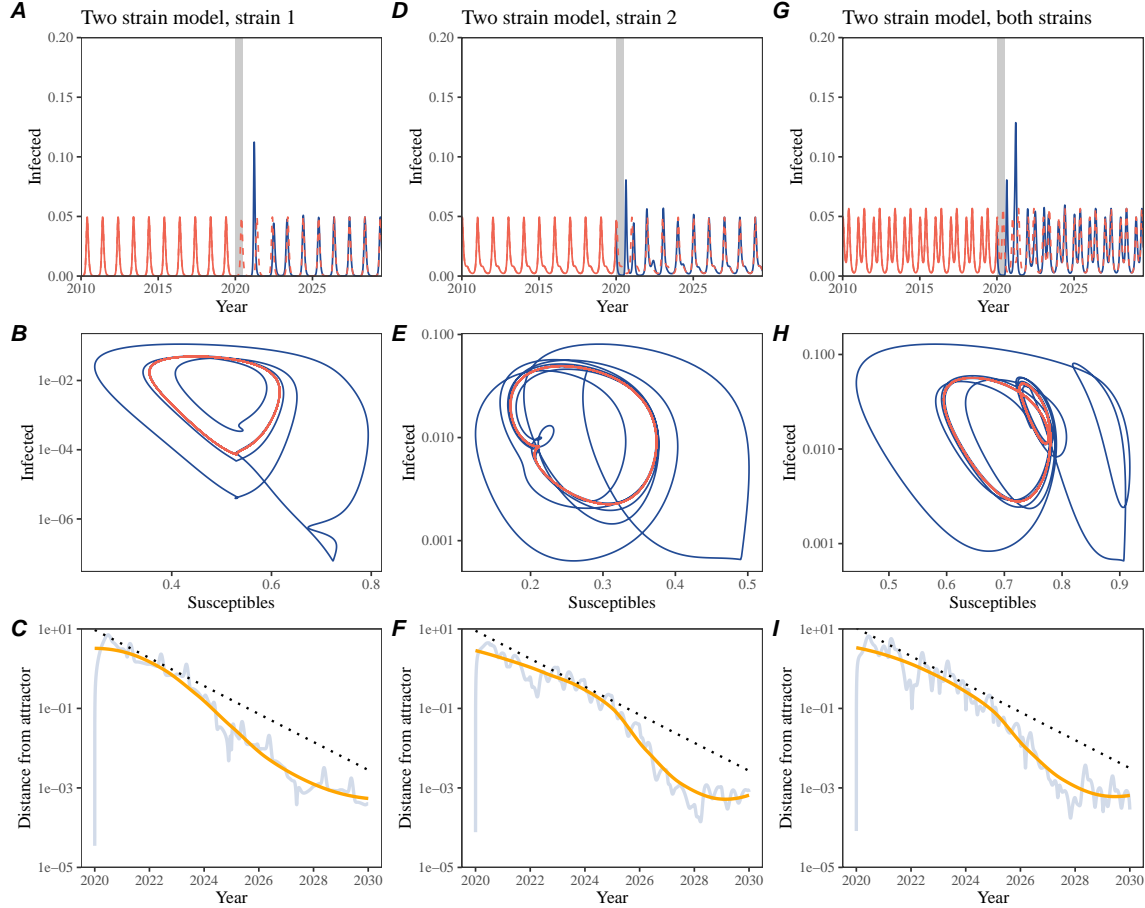


**Figure S3: Conceptual framework for measuring pathogen resilience following NPIs for a two-strain system with seasonal forcing.** (A, D, G) Simulated epidemic trajectories using a two-strain system with seasonal forcing (amplitude of 0.2). In this model, two strains compete through cross immunity. Red and blue solid lines represent epidemic dynamics before and after interventions are introduced, respectively. Red dashed lines represent counterfactual epidemic dynamics in the absence of interventions. Gray regions indicate the duration of interventions. (B, E, H) Phase plane representation of the time series in panels A, D, and G alongside the corresponding susceptible host dynamics. Red and blue solid lines represent epidemic trajectories on an SI phase plane before and after interventions are introduced, respectively. (C, F, I) Changes in logged distance from the attractor over time. Blue lines represent the logged distance from the attractor. Orange lines represent the locally estimated scatterplot smoothing (LOESS) fits to the logged distance from the attractor. Dotted lines show the intrinsic resilience of the seasonally unforced system.

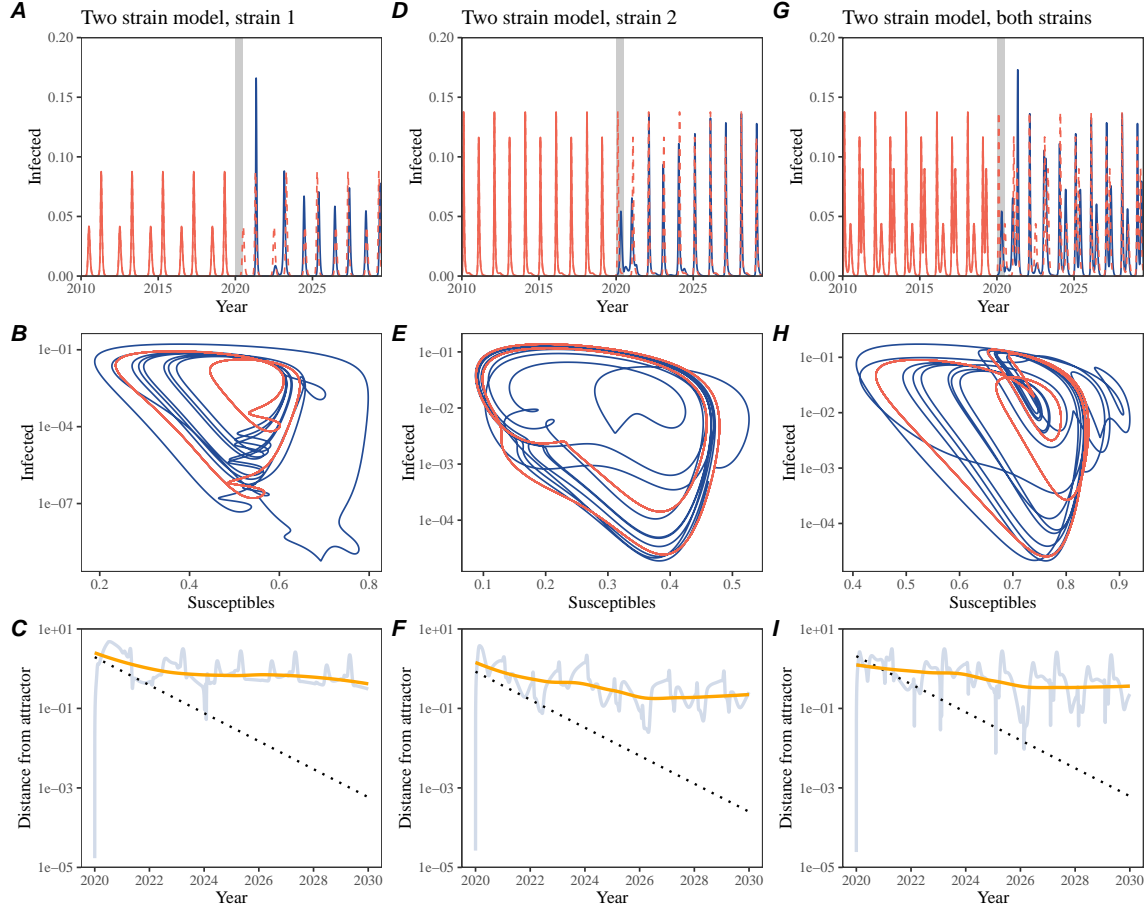


**Figure S4: Conceptual framework for measuring pathogen resilience following NPIs for a multi-strain system with strong seasonal forcing.** (A, D, G) Simulated epidemic trajectories using a multi-strain system with seasonal forcing (amplitude of 0.4). In this model, two strains compete through cross immunity. Red and blue solid lines represent epidemic dynamics before and after interventions are introduced, respectively. Red dashed lines represent counterfactual epidemic dynamics in the absence of interventions. Gray regions indicate the duration of interventions. (B, E, H) Phase plane representation of the time series in panels A, D, and G alongside the corresponding susceptible host dynamics. Red and blue solid lines represent epidemic trajectories on an SI phase plane before and after interventions are introduced, respectively. (C, F, I) Changes in logged distance from the attractor over time. Blue lines represent the logged distance from the attractor. Orange lines represent the locally estimated scatterplot smoothing (LOESS) fits to the logged distance from the attractor. Dotted lines show the intrinsic resilience of the seasonally unforced system.

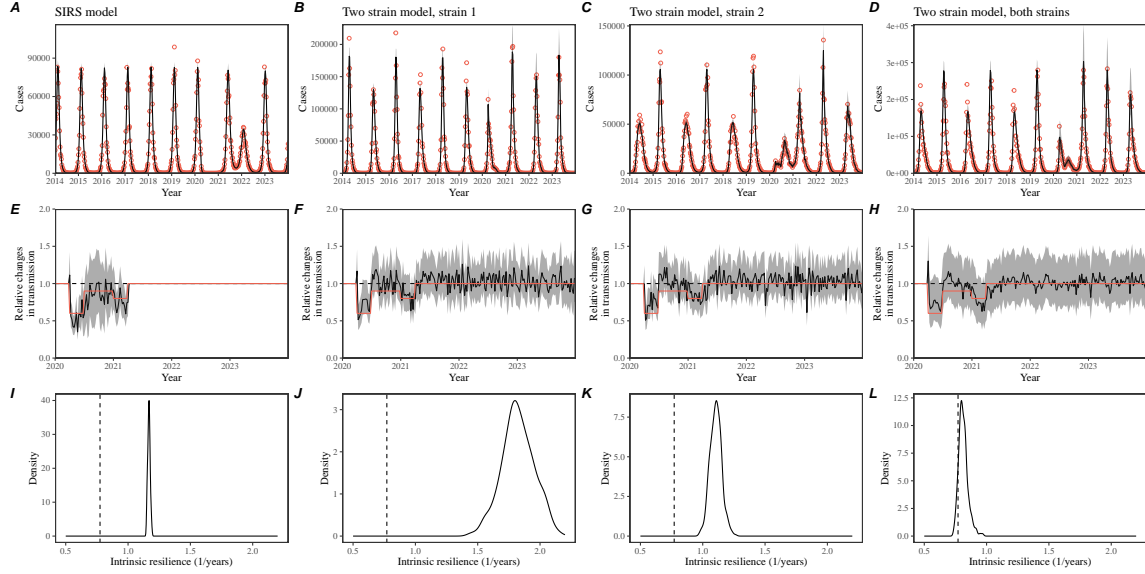


**Figure S5: Mechanistic model fits to simulated data and inferred intrinsic resilience.** We simulated discrete time, stochastic epidemic trajectories using seasonally forced SIRS model (A,E,I) and seasonally forced two-strain model (B–D, F–H, and J–L) and tested whether we can estimate the intrinsic resilience of the seasonally unforced versions of the model by fitting a mechanistic model (Supplementary Text). We fitted the same discrete time, deterministic SIRS model across all four scenarios. (A–D) Simulated case time series from corresponding models shown in the title (red) and SIRS model fits (black). (E–H) Assumed changes in transmission due to pandemic perturbations (red) and estimated time-varying relative transmission rates for the perturbation impact from the SIRS model fits (black). Solid lines and shaded regions represent fitted posterior median and 95% credible intervals. (I–L) True intrinsic resilience of the seasonally unforced system (vertical lines) and the posterior distribution of the inferred intrinsic resilience from the SIRS model (density plots).

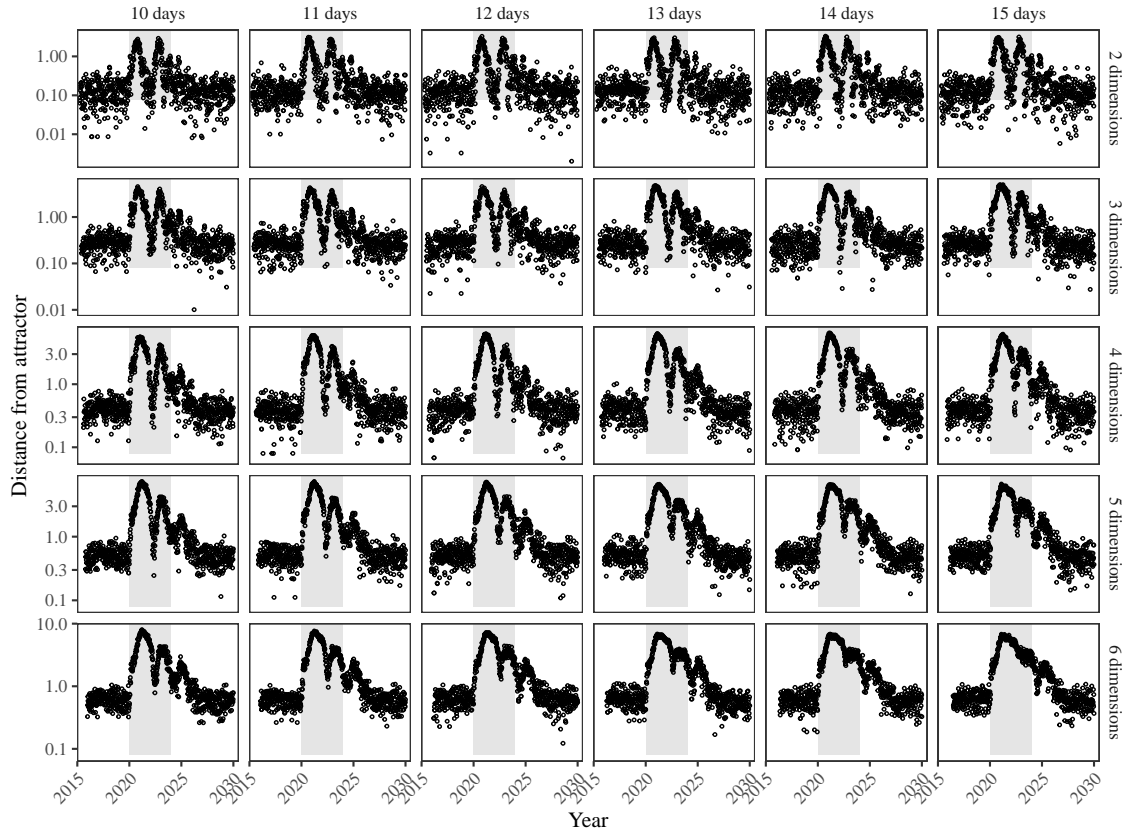


**Figure S6: Sensitivity of the distance from the attractor to choices about embedding lags and dimensions.** Sensitivity analysis for the distance-from-attractor time series shown in Figure 3E in the main text by varying the embedding lag between 10–15 days and embedding dimensions between 2–6 dimensions. [SWP: You said: “Did you do sensitivity analyses with other systems or just this one? I think we’ll probably need to do it with several systems”. I think it’s OK to just do this because we’re just trying to show qualitatively that longer lags and higher dimensions smooth things out. We also explore resilience of other models in other figures.]

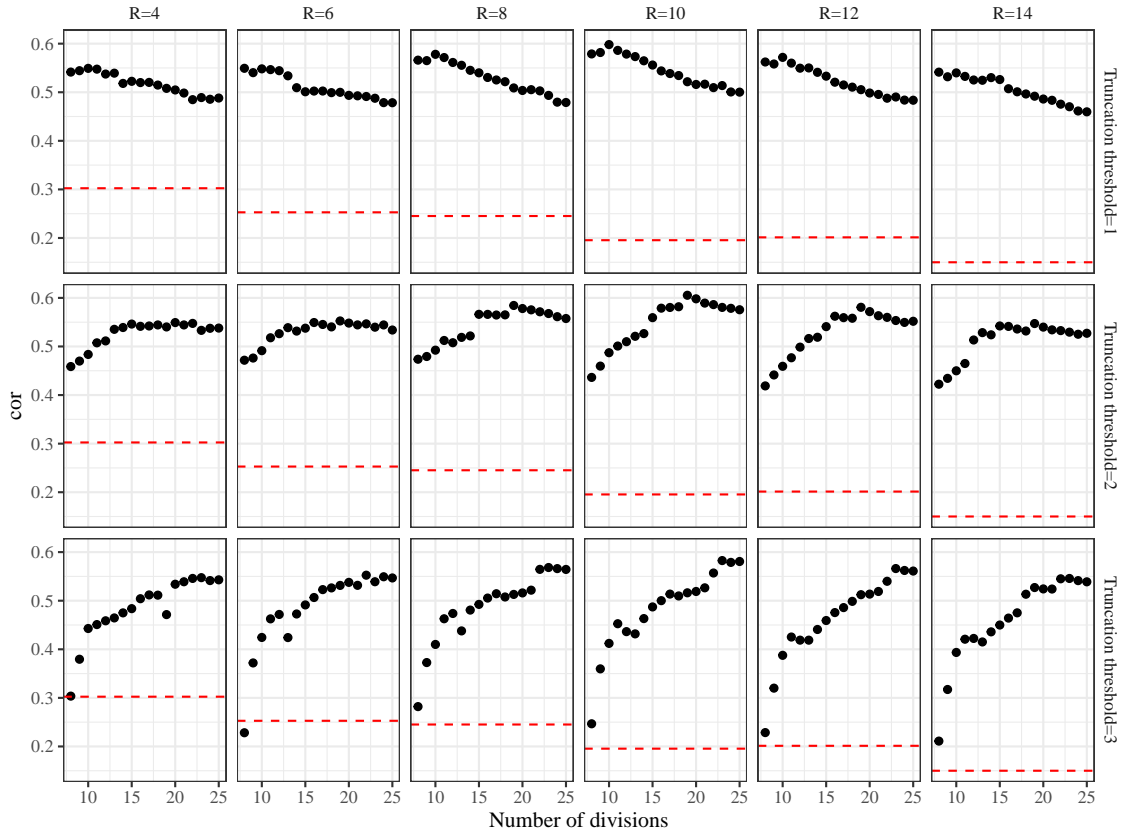


**Figure S7: Impact of fitting window selection on the estimation of empirical resilience.** We simulated 500 epidemics of a stochastic SIRS model with randomly drawn parameters and randomly generated pandemic perturbations (Supplementary Text). For each simulation, we varied the false nearest neighbor threshold  $R$  for reconstructing the empirical attractor as well as the parameters for regression window selection (i.e., the truncation threshold  $a$  and the the number of divisions  $K$ ). Each point represents the resulting correlation coefficient between empirical and intrinsic resilience estimates for a given scenario. Dashed lines represent the correlation coefficient between empirical and intrinsic resilience estimates for the naive approach that fits a linear regression on a log scale, starting from the maximum distance until the end of the time series.

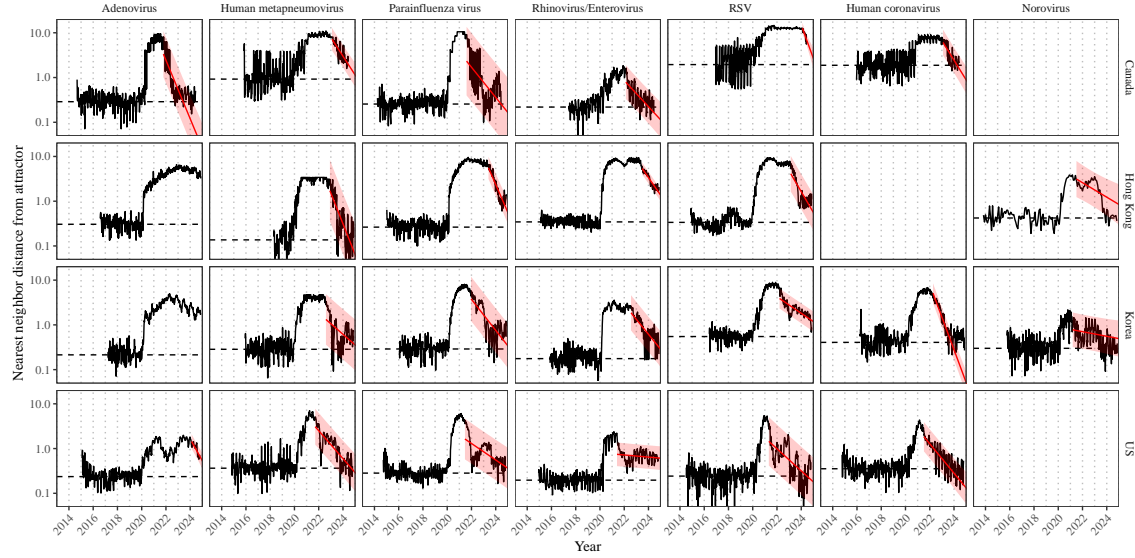


**Figure S8: Estimated time series of distance from the attractor for each pathogen and corresponding linear regression fits using automated window selection criterion across Canada, Hong Kong, Korea, and the US.** Black lines represent the estimated distance from the attractor. Red lines and shaded regions represent the linear regression fits and corresponding 95% confidence intervals. Dashed lines represent the average of the pre-pandemic nearest neighbor distances.

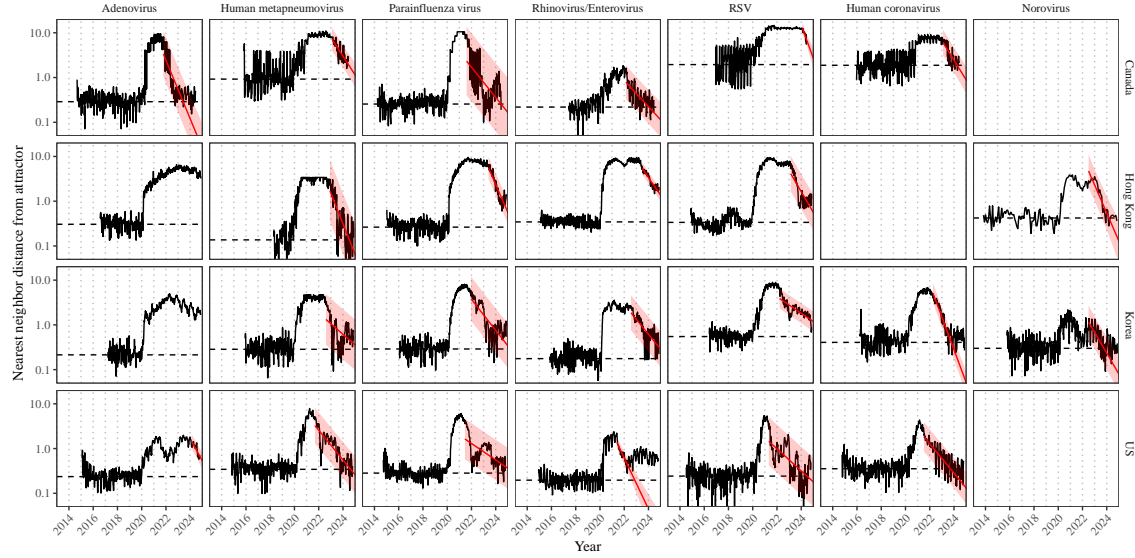


**Figure S9: Estimated time series of distance from the attractor for each pathogen and corresponding linear regression fits across Canada, Hong Kong, Korea, and the US, including ad-hoc regression window selection.** We used ad-hoc regression windows for norovirus in Hong Kong and Korea and Rhinovirus/Enterovirus in the US. Black lines represent the estimated distance from the attractor. Red lines and shaded regions represent the linear regression fits and corresponding 95% confidence intervals. Dashed lines represent the average of the pre-pandemic nearest neighbor distances.

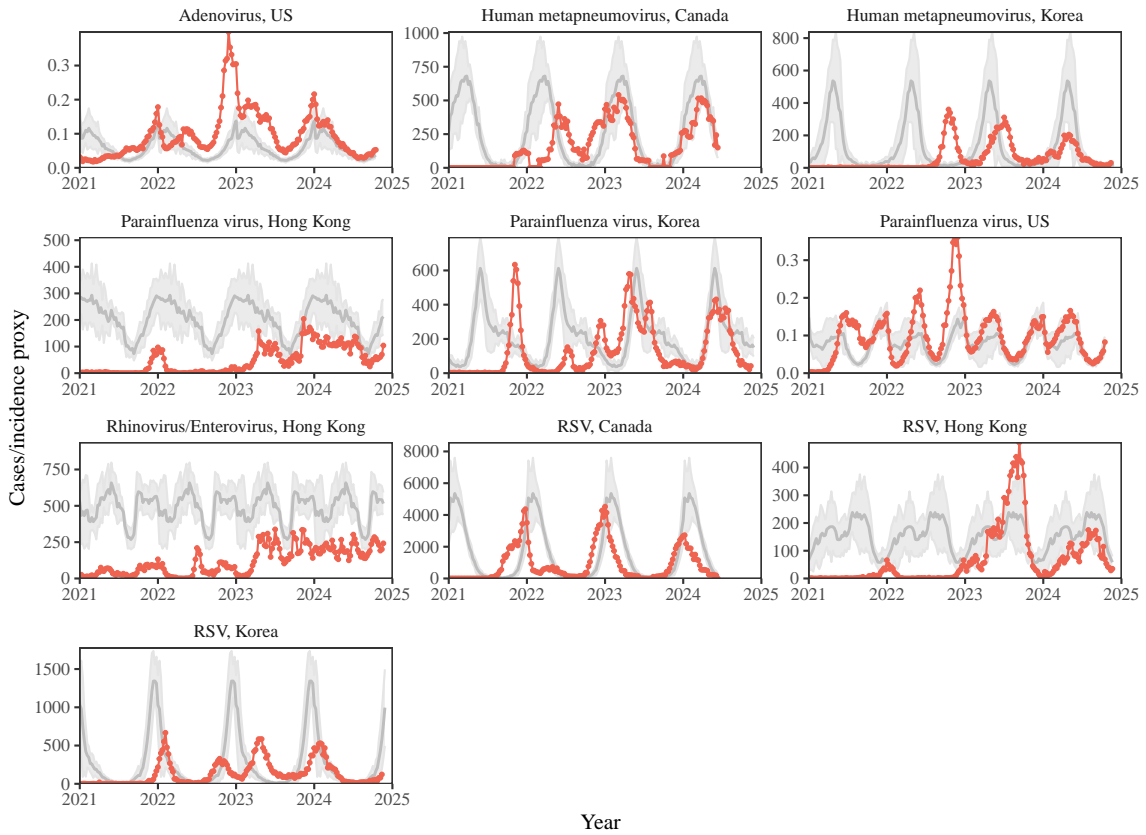


**Figure S10: Observed dynamics for pathogen that are predicted to return after the end of 2024.** Red points and lines represent data before 2020. Gray lines and shaded regions represent the mean seasonal patterns and corresponding 95% confidence intervals around the mean, previously shown in Figure 1.

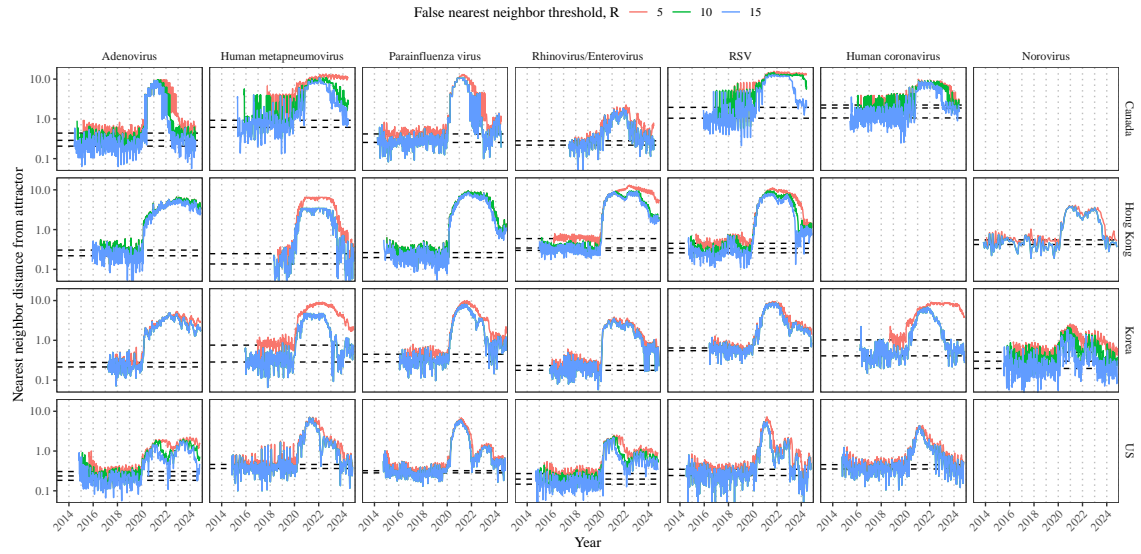


**Figure S11: Estimated time series of distance from the attractor for each pathogen across different choices about false nearest neighbor threshold values.** Using higher threshold values for the false nearest neighbor approach gives lower embedding dimensions. Colored lines represent the estimated distance from the attractor for different threshold values.

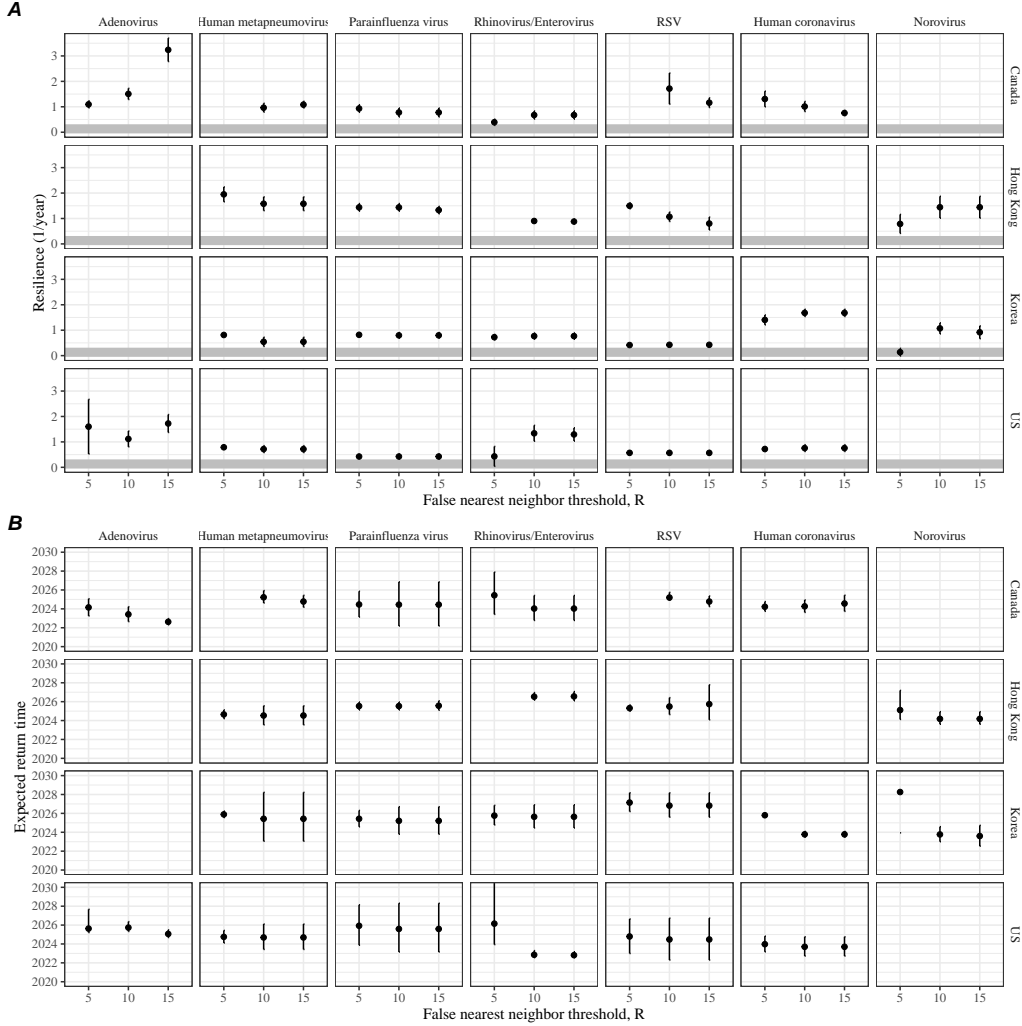


**Figure S12: Summary of resilience estimates and predictions for return time across different choices about false nearest neighbor threshold values.** The automated window selection method was used for all scenarios to estimate pathogen resilience, except for norovirus in Hong Kong and Korea and Rhinovirus/Enterovirus in the US. We used the same ad-hoc regression windows for norovirus in Hong Kong and Korea and Rhinovirus/Enterovirus in the US as we did in the main analysis. (A) Estimated pathogen resilience. The gray horizontal line represents the intrinsic resilience of pre-vaccination measles dynamics. (B) Predicted timing of when each pathogen will return to their pre-pandemic cycles. The dashed line in panel B indicates the end of 2024 (current observation time). Error bars represent 95% confidence intervals.

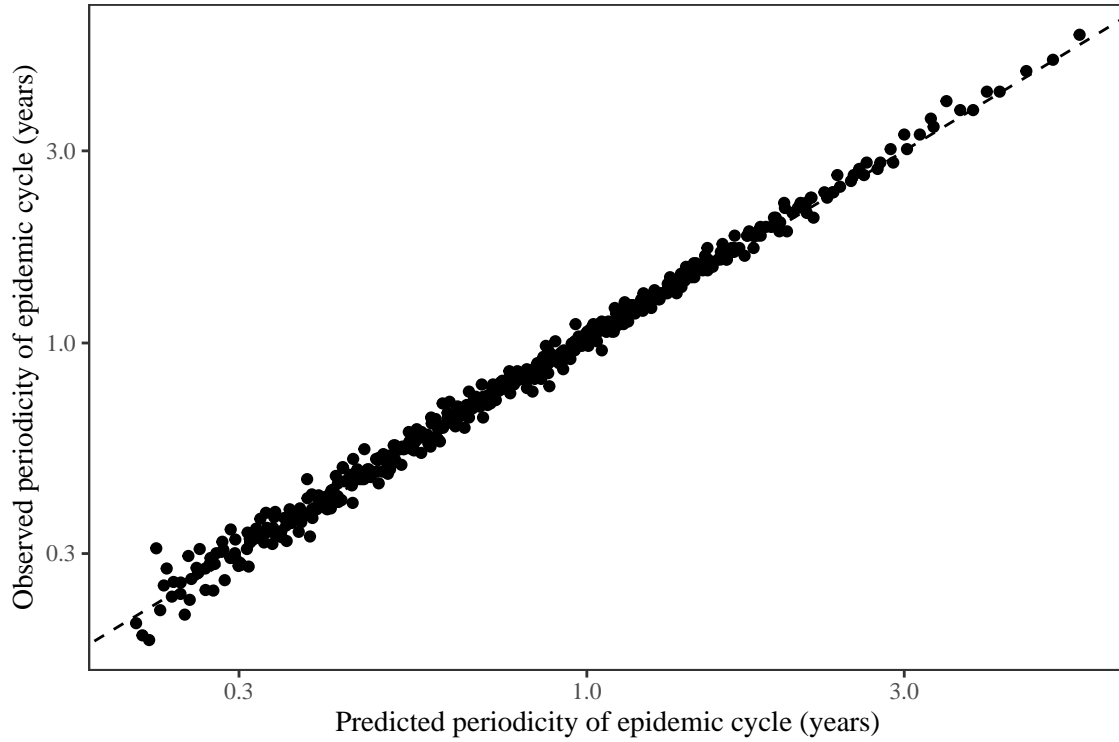
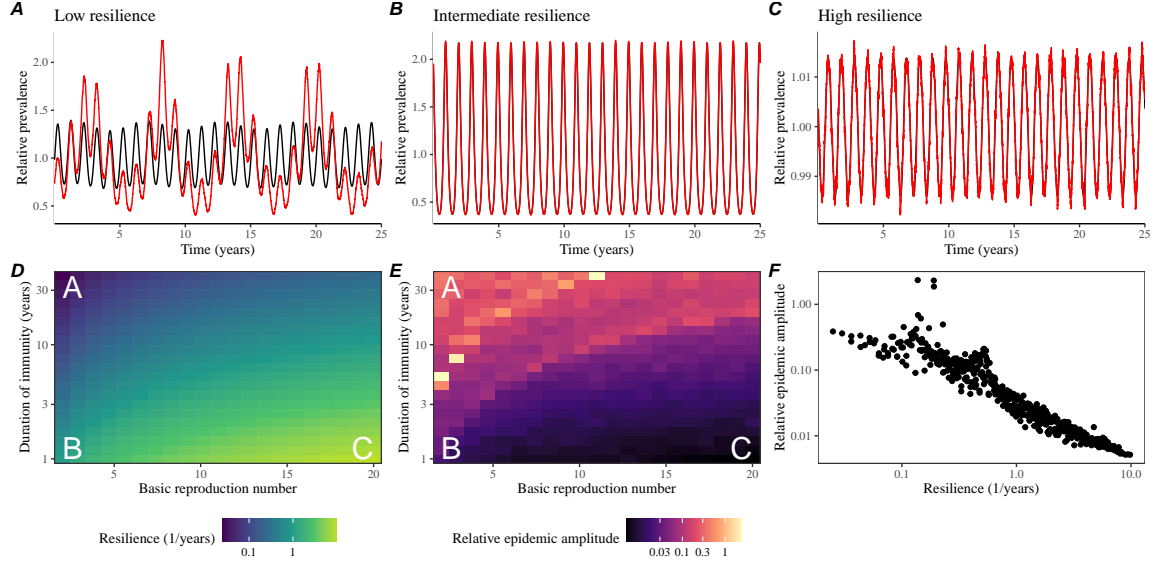


Figure S13: **Comparison between the observed and predicted periodicity of the epidemic cycle of the seasonally unforced SIRS model.** The observed periodicity of the epidemic corresponds to the periodicity at which maximum spectral density occurs. The predicted periodicity of the epidemic corresponds to  $2\pi/\text{Im}(\lambda)$ , where  $\text{Im}(\lambda)$  is the imaginary part of the eigenvalue.



**Figure S14: Linking resilience of a host-pathogen system to its sensitivity to stochastic perturbations for the seasonally forced SIRS model.** (A–C) Epidemic trajectories of a stochastic SIRS model across three different resilience values: low, intermediate, and high. The relative prevalence was calculated by dividing infection prevalence by its mean value. (D) The heat map represents the intrinsic resilience of the seasonally unforced system as a function of the basic reproduction number  $\mathcal{R}_0$  and the duration of immunity. (E) The heat map represents the relative epidemic amplitude as a function of the basic reproduction number  $\mathcal{R}_0$  and the duration of immunity. To calculate the relative epidemic amplitude, we first take the relative difference in infection prevalence between stochastic and deterministic trajectories:  $\epsilon = (I_{\text{stoch}} - I_{\text{det}})/I_{\text{det}}$ . Then, we calculate the difference between maximum and minimum of the relative difference and divide by half:  $(\max \epsilon - \min \epsilon)/2$ . (F) The relationship between pathogen resilience and relative epidemic amplitude.

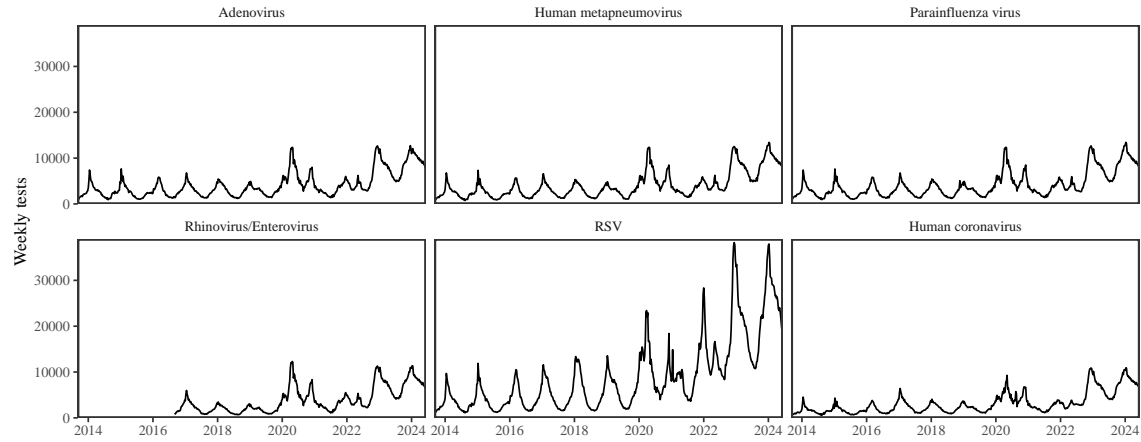


Figure S15: Testing patterns for respiratory pathogens in Canada.

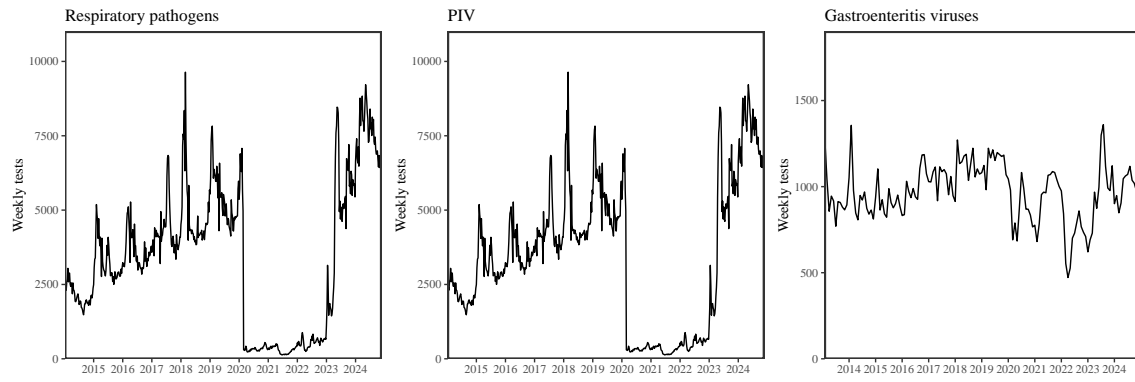


Figure S16: Testing patterns for respiratory pathogens, PIV, and gastroenteritis viruses in Hong Kong.

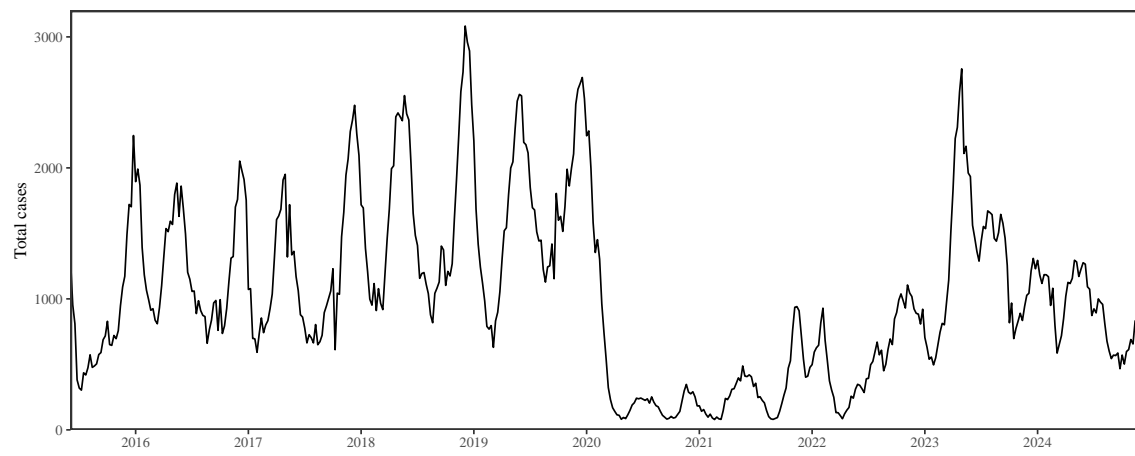


Figure S17: Total number of reported respiratory infection cases in Korea.

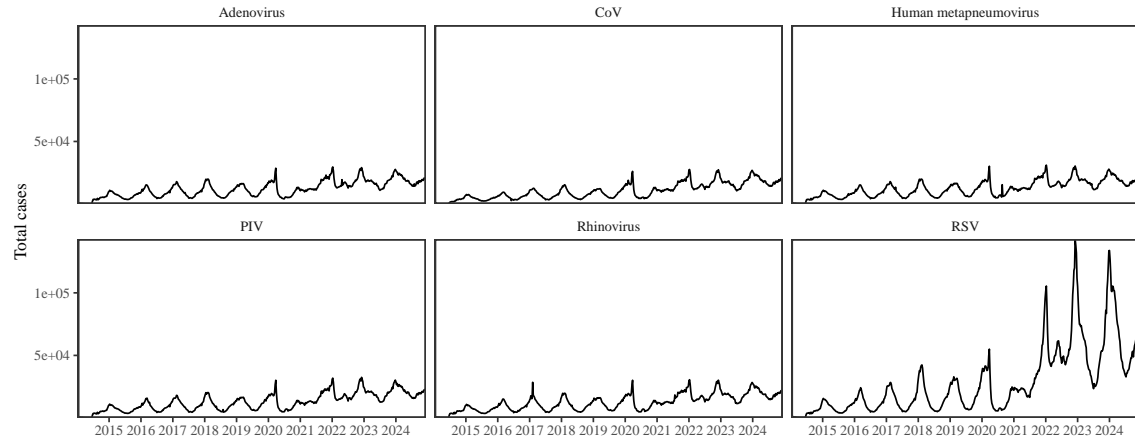


Figure S18: Testing patterns for respiratory pathogens in the US reported through the NREVSS.

## 731 References

- 732 [1] Rachel E Baker, Sang Woo Park, Wenchang Yang, Gabriel A Vecchi, C Jessica E  
733 Metcalf, and Bryan T Grenfell. The impact of COVID-19 nonpharmaceutical  
734 interventions on the future dynamics of endemic infections. *Proceedings of the*  
735 *National Academy of Sciences*, 117(48):30547–30553, 2020.
- 736 [2] Gabriela B Gomez, Cedric Mahé, and Sandra S Chaves. Uncertain effects of the  
737 pandemic on respiratory viruses. *Science*, 372(6546):1043–1044, 2021.
- 738 [3] Mihaly Koltai, Fabienne Krauer, David Hodgson, Edwin van Leeuwen, Marina  
739 Treskova-Schwarzbach, Mark Jit, and Stefan Flasche. Determinants of RSV  
740 epidemiology following suppression through pandemic contact restrictions. *Epi-*  
741 *demics*, 40:100614, 2022.
- 742 [4] Sang Woo Park, Brooklyn Noble, Emily Howerton, Bjarke F Nielsen, Sarah  
743 Lentz, Lilliam Ambroggio, Samuel Dominguez, Kevin Messacar, and Bryan T  
744 Grenfell. Predicting the impact of non-pharmaceutical interventions against  
745 COVID-19 on *Mycoplasma pneumoniae* in the United States. *Epidemics*,  
746 49:100808, 2024.
- 747 [5] Amanda C Perofsky, Chelsea L Hansen, Roy Burstein, Shanda Boyle, Robin  
748 Prentice, Cooper Marshall, David Reinhart, Ben Capodanno, Melissa Truong,  
749 Kristen Schwabe-Fry, et al. Impacts of human mobility on the citywide trans-  
750 mission dynamics of 18 respiratory viruses in pre-and post-COVID-19 pandemic  
751 years. *Nature communications*, 15(1):4164, 2024.
- 752 [6] Eric J Chow, Timothy M Uyeki, and Helen Y Chu. The effects of the COVID-19  
753 pandemic on community respiratory virus activity. *Nature Reviews Microbiol-*  
754 *ogy*, 21(3):195–210, 2023.
- 755 [7] Stephen M Kissler, Christine Tedijanto, Edward Goldstein, Yonatan H Grad,  
756 and Marc Lipsitch. Projecting the transmission dynamics of SARS-CoV-2  
757 through the postpandemic period. *Science*, 368(6493):860–868, 2020.
- 758 [8] Rachel E Baker, Chadi M Saad-Roy, Sang Woo Park, Jeremy Farrar, C Jessica E  
759 Metcalf, and Bryan T Grenfell. Long-term benefits of nonpharmaceutical inter-  
760 ventions for endemic infections are shaped by respiratory pathogen dynamics.  
761 *Proceedings of the National Academy of Sciences*, 119(49):e2208895119, 2022.
- 762 [9] John-Sebastian Eden, Chisha Sikazwe, Ruopeng Xie, Yi-Mo Deng, Sheena G  
763 Sullivan, Alice Michie, Avram Levy, Elena Cutmore, Christopher C Blyth,  
764 Philip N Britton, et al. Off-season RSV epidemics in Australia after easing  
765 of COVID-19 restrictions. *Nature communications*, 13(1):2884, 2022.
- 766 [10] Stuart L Pimm. The structure of food webs. *Theoretical population biology*,  
767 16(2):144–158, 1979.

- 768 [11] Michael G Neubert and Hal Caswell. Alternatives to resilience for measuring  
769 the responses of ecological systems to perturbations. *Ecology*, 78(3):653–665,  
770 1997.
- 771 [12] Lance H Gunderson. Ecological resilience—in theory and application. *Annual  
772 review of ecology and systematics*, 31(1):425–439, 2000.
- 773 [13] Vasilis Dakos and Sonia Kéfi. Ecological resilience: what to measure and how.  
774 *Environmental Research Letters*, 17(4):043003, 2022.
- 775 [14] Floris Takens. Detecting strange attractors in turbulence. In *Dynamical Sys-  
776 tems and Turbulence, Warwick 1980: proceedings of a symposium held at the  
777 University of Warwick 1979/80*, pages 366–381. Springer, 2006.
- 778 [15] Jonathan Dushoff, Joshua B Plotkin, Simon A Levin, and David JD Earn. Dynamical resonance can account for seasonality of influenza epidemics. *Pro-  
779 ceedings of the National Academy of Sciences*, 101(48):16915–16916, 2004.
- 780 [16] Alan Hastings, Karen C Abbott, Kim Cuddington, Tessa Francis, Gabriel Gell-  
781 ner, Ying-Cheng Lai, Andrew Morozov, Sergei Petrovskii, Katherine Scran-  
782 ton, and Mary Lou Zeeman. Transient phenomena in ecology. *Science*,  
783 361(6406):eaat6412, 2018.
- 784 [17] Matthew B Kennel, Reggie Brown, and Henry DI Abarbanel. Determining  
785 embedding dimension for phase-space reconstruction using a geometrical con-  
786 struction. *Physical review A*, 45(6):3403, 1992.
- 787 [18] Eugene Tan, Shannon Algar, Débora Corrêa, Michael Small, Thomas Stemler,  
788 and David Walker. Selecting embedding delays: An overview of embedding  
789 techniques and a new method using persistent homology. *Chaos: An Interdis-  
790 ciplinary Journal of Nonlinear Science*, 33(3), 2023.
- 791 [19] Jennifer M Radin, Anthony W Hawksworth, Peter E Kammerer, Melinda Bal-  
792 ansay, Rema Raman, Suzanne P Lindsay, and Gary T Brice. Epidemiology  
793 of pathogen-specific respiratory infections among three US populations. *PLoS  
794 One*, 9(12):e114871, 2014.
- 795 [20] Guojian Lv, Limei Shi, Yi Liu, Xuecheng Sun, and Kai Mu. Epidemiological  
796 characteristics of common respiratory pathogens in children. *Scientific Reports*,  
797 14(1):16299, 2024.
- 798 [21] Saverio Caini, Adam Meijer, Marta C Nunes, Laetitia Henaff, Malaika Zounon,  
799 Bronke Boudewijns, Marco Del Riccio, and John Paget. Probable extinction of  
800 influenza b/yamagata and its public health implications: a systematic literature  
801 review and assessment of global surveillance databases. *The Lancet Microbe*,  
802 2024.

- 804 [22] Zhiyuan Chen, Joseph L-H Tsui, Bernardo Gutierrez, Simon Busch Moreno,  
805 Louis du Plessis, Xiaowei Deng, Jun Cai, Sumali Bajaj, Marc A Suchard,  
806 Oliver G Pybus, et al. COVID-19 pandemic interventions reshaped the global  
807 dispersal of seasonal influenza viruses. *Science*, 386(6722):eadq3003, 2024.
- 808 [23] Bryan T Grenfell, Ottar N Bjørnstad, and Bärbel F Finkenstädt. Dynamics of  
809 measles epidemics: scaling noise, determinism, and predictability with the TSIR  
810 model. *Ecological monographs*, 72(2):185–202, 2002.
- 811 [24] Samit Bhattacharyya, Per H Gesteland, Kent Korgenski, Ottar N Bjørnstad,  
812 and Frederick R Adler. Cross-immunity between strains explains the dynamical  
813 pattern of paramyxoviruses. *Proceedings of the National Academy of Sciences*,  
814 112(43):13396–13400, 2015.
- 815 [25] Virginia E Pitzer, Cécile Viboud, Wladimir J Alonso, Tanya Wilcox, C Jessica  
816 Metcalf, Claudia A Steiner, Amber K Haynes, and Bryan T Grenfell. Environmental  
817 drivers of the spatiotemporal dynamics of respiratory syncytial virus in  
818 the United States. *PLoS pathogens*, 11(1):e1004591, 2015.
- 819 [26] Katharine R Dean, Fabienne Krauer, Lars Walløe, Ole Christian Lingjærde, Bar-  
820 bara Bramanti, Nils Chr Stenseth, and Boris V Schmid. Human ectoparasites  
821 and the spread of plague in Europe during the Second Pandemic. *Proceedings  
822 of the National Academy of Sciences*, 115(6):1304–1309, 2018.
- 823 [27] Margarita Pons-Salort and Nicholas C Grassly. Serotype-specific immunity  
824 explains the incidence of diseases caused by human enteroviruses. *Science*,  
825 361(6404):800–803, 2018.
- 826 [28] Sarah Cobey and Edward B Baskerville. Limits to causal inference with state-  
827 space reconstruction for infectious disease. *PloS one*, 11(12):e0169050, 2016.
- 828 [29] Public Health Agency of Canada. Respiratory virus detections in  
829 Canada. 2024. <https://www.canada.ca/en/public-health/services/surveillance/respiratory-virus-detections-canada.html>. Accessed Sep  
830 4, 2024.
- 831 [30] Centre for Health Protection. Detection of pathogens from respiratory spec-  
imens. 2024. <https://www.chp.gov.hk/en/statistics/data/10/641/642/2274.html>. Accessed Nov 20, 2024.
- 832 [31] Centre for Health Protection. Detection of gastroenteritis viruses from faecal  
specimens. 2024. <https://www.chp.gov.hk/en/statistics/data/10/641/717/3957.html>. Accessed Nov 20, 2024.
- 833 [32] Korea Disease Control and Prevention Agency. Acute respiratory infection,  
834 Sentinel surveillance infectious diseases. 2024. <https://dportal.kdca.go.kr/pot/is/st/ari.do>. Accessed Nov 20, 2024.

- 841 [33] Edward Goldstein, Sarah Cobey, Saki Takahashi, Joel C Miller, and Marc Lip-  
842 sitch. Predicting the epidemic sizes of influenza A/H1N1, A/H3N2, and B: a  
843 statistical method. *PLoS medicine*, 8(7):e1001051, 2011.
- 844 [34] Bob Carpenter, Andrew Gelman, Matthew D Hoffman, Daniel Lee, Ben  
845 Goodrich, Michael Betancourt, Marcus A Brubaker, Jiqiang Guo, Peter Li,  
846 and Allen Riddell. Stan: A probabilistic programming language. *Journal of*  
847 *statistical software*, 76, 2017.
- 848 [35] Stan Development Team. RStan: the R interface to Stan, 2024. R package  
849 version 2.32.6.